

Phase Transition in a Memristive Suspended MoS₂ Monolayer Probed by Opto- and Electro-Mechanics.

Julien Chaste^{1*}, Imen Hnid¹, Lama Khalil¹, Chen Si², Alan Durnez¹, Xavier Lafosse¹, Meng-Qiang Zhao³, A.T. Charlie Johnson³, Shengbai Zhang⁴, Junhyeok Bang^{5**}, Abdelkarim Ouerghi¹

¹Université Paris-Saclay, CNRS, Centre de Nanosciences et de Nanotechnologies, 91120, Palaiseau, France.

² School of Materials Science and Engineering, Beihang University, Beijing 100191, China

³ Department of Physics and Astronomy, University of Pennsylvania, 209S 33rd Street, Philadelphia, Pennsylvania 19104 6396, United States

⁴ Department of Physics, Applied Physics, & Astronomy, Rensselaer Polytechnic Institute, Troy, New York 12180, USA

⁵ Department of Physics, Chungbuk National University, Cheongju 28644, Republic of Korea

* Corresponding author: julien.chaste@universite-paris-saclay.fr

* Corresponding for theory: jbang@cbnu.ac.kr

Abstract

Semiconducting monolayer of 2D material are able to concatenate multiple interesting properties into a single component. Here, by combining opto-mechanical and electronic measurements, we demonstrate the presence of a partial 2H-1T' phase transition in a suspended 2D monolayer membrane of MoS₂. Electronic transport shows unexpected memristive properties in the MoS₂ membrane, in the absence of any external dopants. A strong mechanical softening of the membrane is measured concurrently and may only be related to the phase 2H-1T' phase transition which imposes a 3% directional elongation of the topological 1T' phase with respect to the semiconducting 2H. We note that only a few percent 2H-1T' phase switching is sufficient to observe measurable memristive effects. Our experimental results combined with First-principles total energy calculations indicate that sulfur vacancy diffusion plays a key role in the initial nucleation of the phase transition. Our study clearly shows that nanomechanics represents an ultrasensitive technique to probe the crystal phase transition in 2D materials or thin membranes. Finally, a better control of the microscopic mechanisms responsible for the observed memristive effect in MoS₂ is important for the implementation of future devices.

Keyword; 2D materials, memristor, nanomechanic, photocurrent, phase transition

Semiconducting two-dimensional transition metal dichalcogenides (2D TMDs) are promising candidates for optoelectronic devices and electronic transistors.^{1,2} Their 2D nature strongly affects the value of the excitonic binding energy,³ spin-orbit coupling,⁴ and energy band gap.⁵ These substantial changes of the electronic characteristics turn 2D MoS₂ in a versatile material which combines multiple interesting properties. For example, 2D MoS₂ has been recently investigated both for memristive devices.^{6,7} and energy storage applications.⁸⁻¹¹

A memristor is a circuit element¹² combining both memory and transduction¹³. Most memristor relies on dopant migration to alter their electronic properties, *e.g.* Li⁺ ion migration in multilayer MoS₂ or oxide vacancies in TiO₂¹³. For multilayer MoS₂, a strong doping due to the intercalation of 0.4 Li atom per unit cell can induce a crystal phase transition between the 1T' and 2H crystalline phases of the 2D TMD material,¹⁴ and thereby creating interesting memristive phenomena. In the absence of strong dopants, other memristive effects have been observed in lateral⁶ and vertical MoS₂-based transistors.^{9,15} and linked to the migration of grain boundaries and sulfur vacancies (S_V). However it is unclear if those models can apply to the simple case of a single monocrystalline MoS₂ flake of monolayer thickness, for which grain boundaries and intercalation phenomena are absent.

Standard characterization methods, such as Raman spectroscopy,¹⁶ photoemission spectroscopy or transmission electron microscopy (TEM),^{17,8} have been employed to study both 2H and 1T' phases in TMDs. However, all these methods present some drawbacks, and they are difficult to combine with *in situ* electrical measurements of the memristive effect. For example, TEM unambiguously discriminates the 2H and 1T' phases but it is restricted to a small area and can affect the dynamics of crystal phase transition depending on the beam excitation. Similarly, optical methods based on lasers can also induced such artefacts with power above 100μW¹⁸. Consequently, there is a need for atypical characterization methods, which can observe and probe both the phase transition and the vacancy migration in TMDs in a non-disturbing manner. Since flexural vibrations are very sensitive to force, crystal distortion, charge or atoms absorption,¹⁹ an appropriate way to explore in detail the behaviors of 2D TMDs is nanomechanics. The emergence of suspended materials with a single-atom thickness²⁰ brought interesting properties for nanomechanical resonators including very low mass and stiffness constants,²¹ high resistance to elongation, variable frequency, and strong mechanical non-linearities.²² Nanomechanical resonators made of ultrathin suspended monolayers of TMDs²³⁻²⁶ may be less studied than their graphene counterparts, but they are also more suitable for technological applications.

In this work, we probe by nanomechanics the memristive properties of a suspended monocrystalline MoS₂ flake of monolayer thickness which has a high density of S_V defects (10-18%, determined in a previous report)²⁷. The device exhibits persistent photocurrents (PPCs) related to S_V dopants and their slow diffusion on few micrometers. This scenario is totally different when probed at the nanometer scale and our findings unveil that S vacancies have a faster and high in-plane diffusivity, and that they can promote the nucleation of the 1T' phase. With a simple voltage and optical excitation, we are able to control the S_V drift over nanometric scales, it is enough to imply a phase transition and a resulting memristive effect. These results are confirmed by first-principles total energy calculations, which show that the optical excitation can significantly enhance the S_V diffusion and accelerate the phase transition from the 2H phase to the 1T' one. This phase transition was only detected for a very small part of the material with a strong softening of the membrane.

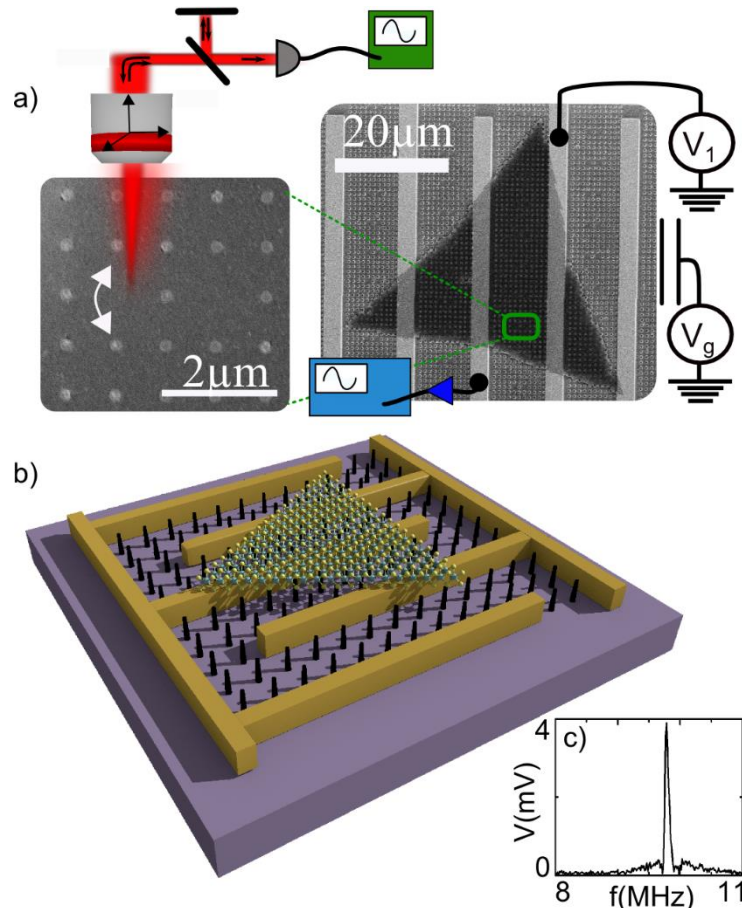


Figure 1 Optomechanical and electrical set-up for the suspended MoS₂ membrane. a) Electronic image of a monolayer MoS₂ suspended between interdigitated contacts and an array of SiO₂ nanopillars. It resulted in a periodic series of local mechanical oscillators. The vibration was excited with an electrostatic back-gate and measured with a reflective laser (633nm,) using a Michelson interferometer. b) Schematic of the sample showing the MoS₂ flake suspended above the pillar array. c) Typical mechanical resonance measurement.

Results and discussions

Figure 1a presents the geometry of our monocrystalline single-layer MoS₂ flake, grown by chemical vapor deposition (CVD),²⁸ suspended on an array of SiO₂ pillars and interdigitated electrical contacts. The specimen was embedded in a nano-opto-electro-mechanical system which uses electrocapacitive excitations to induce periodic mechanical vibrations in the MoS₂ monolayer, finally detected by optical interferometry (Figure 1b). The arrangement of the metallic electrodes and SiO₂ substrate provides the electrostatic gating of the MoS₂ flake. We measure the vertical motion of the membrane with a reflected laser signal and its vibrations by means of a Michelson interferometer, as shown in Figure 1a. We observe mechanical oscillations centered at $f_0 = 1/2\pi \sqrt{k/m}$ at ~ 10 MHz with k and m the resonator spring constant and the effective mass of the resonator, respectively. The resonance quality factor (Q) is 320 at room temperature, in agreement with our previous report.²⁹

The electrical transport properties of the suspended MoS₂ film were then investigated for different fluence of a red laser source (Figure 2a). We notice that the conductance is enhanced with increasing laser power due to a photodoping effect related to the presence of in-gap states in MoS₂.³⁰ Without any light, a robust persistent photocurrent remains present for few hours in our sample.

Beside this persistent photocurrent, the other feature is a clear hysteretic loop in I - V when V_{ds} is swept back and forth from $-7V$ to $7V$, which reflects a nonlinear memristive behavior of our system. The current sweeps between two states 0 and 1 at a threshold voltage V_H and at a current step ΔI_H . Note that our device is electrically bipolar (see Supplementary Information Figure S1).

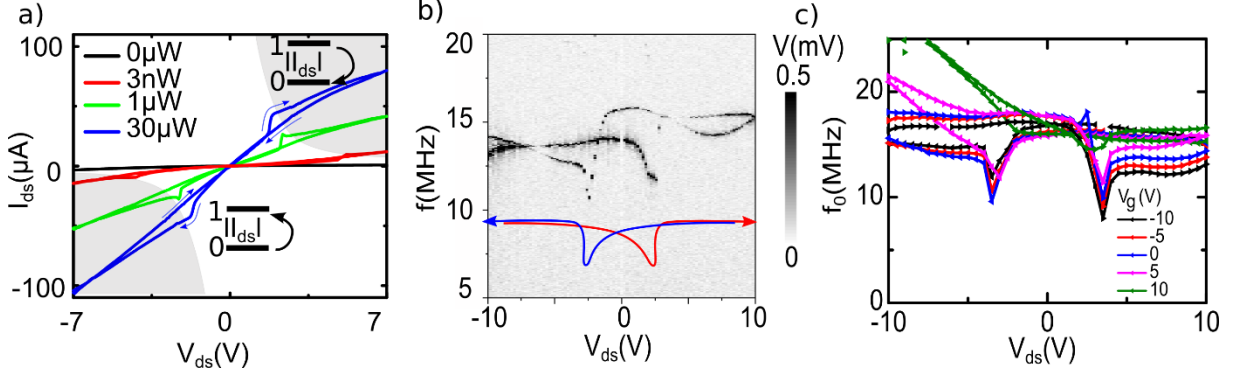


Figure 2 Memristive behavior of the MoS₂ for both current and mechanical resonance as a function of V_{ds} . a) The $I_{ds}(V_{ds})$ for both sweep directions and for different laser powers presents a clear hysteresis and memristive property. In the white (grey) region, the current tended to increase (decrease) along the time sweep, at fix V_{ds} , and the memristor current went from state 0 to 1 (1 to 0). b) The laser reflection displayed an optomechanical response to an electrical excitation at frequency f and was traced as a function of V_{ds} for both sweep directions. We observed a variation of the resonant frequency f_0 with a hysteresis along V_{ds} and a strong softening of the mechanical mode. The frequency was reduced by half in this case at the same polarization as the memristive effect. Red and blue lines have been drawn for clarity. c) The mechanical frequency of the same resonator as a function of V_{ds} for different back-gate voltage.

Further insights into these memristive effects, can be obtained by performing nanomechanical measurements.. Figures 2b and 2c reveal the mechanical resonance as a function of V_{ds} . As one can see, the mechanical mode in the hysteretic loop displays a strong softening, attributed to the memristive behavior of MoS₂ at $\pm V_H$. In addition, the resonant frequency at $V_{ds} = 0V$ is reduced by more than two times with respect to the minimum frequency, f_{min} (Figure 2c); the ratio $f_{0,V_{ds} = 0V}/f_{min}$ was determined to be equal to 2.7 (see Supplementary Information Figure S2a). In contrast to the electronic, the mechanical softening seems here unipolar (see Supplementary Information Figure S2c). Since we have previously measured the strain in our MoS₂ membrane equal to 0.05%,²⁹ the motion can be described

within the stress limit, and hence the frequency is of the form $f_0 = 1/2\pi \cdot \sqrt{2.4048^2 \cdot T / (R^2 \rho)}$

where $\rho = 3073 \text{ kg}\cdot\text{m}^{-2}$ refers to the 2D mass density of MoS₂, R is the radius of the membrane, and T is the total stress (in N/m) applied at the end of the membrane. Only one explanation is relevant here; a 2H-1T' phase transition of only 1% is capable of inducing this strong softening and is sufficient to reduce the total deformation of the membrane to zero. Also, this transition, 2H-1T' naturally yields a shift of conductance, from a high gap to a small gap semiconductor, as obtained in the electrical measurements. In contrast, S_V centers are assumed to stress locally on the material³¹, which is in contradiction with our observations. A downshift of the frequency related to the mass is excluded, see S4. In Figure 2c, besides, the lack in the gate voltage dependence at V_H strongly suggests that the memristive effect is not a capacitive coupling (see Supplementary Information Figure S4).

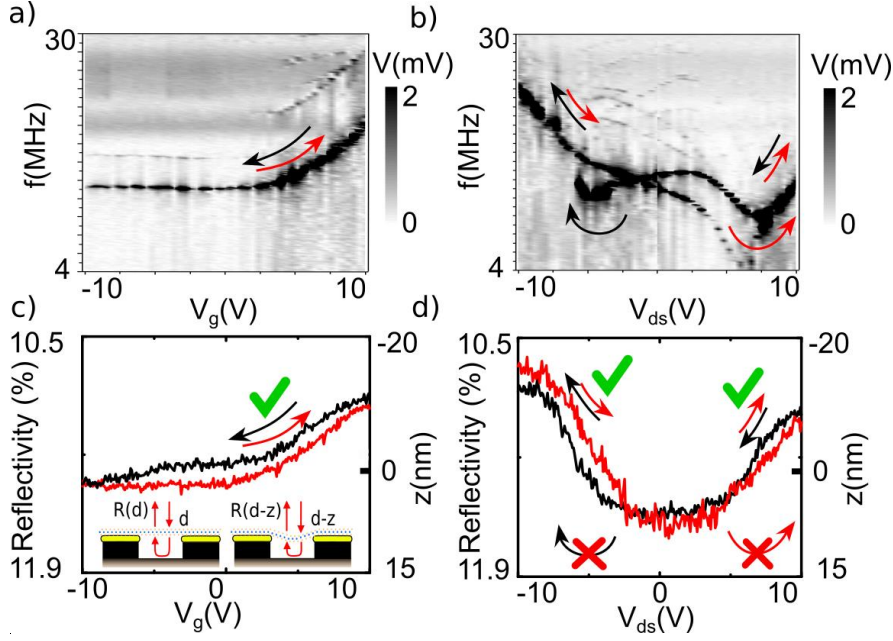


Figure 3 Strain engineering in MoS₂ . We measured the optomechanical response for V_g (a) and V_{ds} (b) and the two sweeping directions. The optical reflectance (633nm) in percent of the input power as a function of V_g (c) ($V_{ds}=-5V$) and V_{ds} (d) ($V_g=4V$) for both sweeping directions (the black curve corresponds to a decreasing potential and the red curve to an increasing one). Inset: schematic of the capacitive electrostatic force applied to the 2D membrane, the reflectivity changes with the distance d when a potential is applied. Both measurements displayed similar dependencies but the hysteresis in V_{ds} , corresponding to the memristive effect, was not present in the reflectance. The same optomechanical measurements were performed before and after the reflectance measurements to confirm that it was not an artifact or a deviation of the xyz position.

To confirm that MoS₂ exhibits a phase transition, which create a stress in the membrane plane, we described our resonator as a circular membrane with clamped sides. We considered the total stress to be $T(z)=T_0+T_D(z)$, where T_0 is the built-in stress and T_D is the stress due to any deflection induced by electrostatic forces. We defined z as the deflection at the center of our circular membrane ($r = 0$). The frequency for the fundamental mode, given by the Euler-Bernoulli description, is defined by (see Supplementary Information Figure S3):

$$f_0 = \frac{1}{2\pi} \sqrt{2.405^4 \frac{Et^3}{12(1-\nu^2)R^4\rho} + 2.405^2 \frac{T_0}{R^2\rho} + 2.405^2 \frac{12}{3} \frac{Et}{(1-\nu^2)} \frac{z(V'_g)^2}{R^4\rho} - 1.23 \frac{\epsilon_0 V'_g{}^2}{d^3\rho}} \quad (1)$$

We define ν as the Poisson ratio, E the Young modulus of the material and ϵ_0 its permittivity. V'_g is a renormalized gate potential, $V'_g \sim V_g - V_{ds}/2 - \mu/e$, where μ is the chemical potential of the MoS₂ and e the elementary charge. It is noteworthy that the first term in Et^3 , *i.e.* the material bending is negligible (~ 200 kHz in our conditions). The second one in T_0 corresponds to the in plane built-in stress of the membrane, and the last two involve a capacitive pull-in (V'_g) with the out of plane deflection (see Supplementary Information Figure S4).

In order to differentiate the in-plane from out of plane movements, we have measured the z variation along the sample by optical reflectometry. The optical cavity formed by the suspended MoS₂ and the silica substrate is of bad quality, but we still manage to measure a deflection along z with approximately 0.04% per nm change of the reflectivity signal (see Supplementary Information Figure S5). In Figure 3, we acquire simultaneously the mechanical

frequency (Figure 3.a-b) and the laser reflectivity (Figure 3.c-d), as a function of V_g and V_{ds} , in the same conditions. We first observe a vertical deflection of 10-20 nm for high V_{ds} and V_g in both sweep directions (Figure 3.c-d). A membrane hardening corresponding to the third term in equation 1.

Surprisingly, , while the memristive softened mode is well visible in the mechanical resonance (Figure 3b), no corresponding signature appears in the vertical (Figure 3d). In the regime dominated by an in-plane intrinsic strain at $V_{ds} \sim V_g = 0$, the static deflection is $z \approx 0$ nm. The modification of this in-plane strain does not affect z and the reflectance, but only the dynamical oscillating deflection $z_{AC}(t)$ resulting from the forced vibration. Therefore, we can conclude that the memristive visible in the mechanical resonance is related to an in plane deformation of the membrane, as in the case of the 2H-1T' phase transition of MoS₂.

Previous investigations have shown that the migration, diffusion or/and clustering of S_v defects are at the heart of memristive behaviors,^{6,15,32} photodoping³⁰ and the 2H-1T' phase transition^{8,31} in MoS₂. The presence of such abundant and stable S_v vacancies can create localized in-gap states and thus a n -type doping in the layer,²⁷ in which the injection is of 0.04e per vacancy.³¹ Obviously, for our suspended membrane, persistent photocurrents (PPCs) are not related to the substrate,^{33,34} but to intrinsic defects, *i.e.* S_v centers. Therefore the measurement of those PPCs can help to understand the dynamics of S_v vacancies over a long time scales (around 500s)^{30,35} and migration length (typically 1 μ m). We have probed the PPCs for different voltages V_{ds} in Figure 4j (see also Supplementary Information Figure S7). The normalized I_{ds} curves were fitted with a sum of exponential functions $I(t) = I_1 e^{-t/\tau_1} + I_2 e^{-t/\tau_2} + \Delta I e^{-t/\tau_3}$, where τ_1 and τ_2 are the characteristic decay times related to two different types of charge traps in MoS₂^{33,34} ($\tau_1 = 269 \pm 48$ s and $\tau_2 = 8815 \pm 690$ s). τ_3 , on the other hand, is much faster and relates to the memristive effect ($\tau_3 \sim 20$ s) and is only included if $V_{ds} > V_H$.

In Figure 4i, we observe a similar current ΔI when the light is ON but greatly hidden by the photocurrent I_{photo} . We found a solution to highlight this effect; we explore the long-time behavior of vibrations. Since we attribute this effect and PPC to vacancies which tends to strain mechanically the MoS₂, it seems quite a natural method.

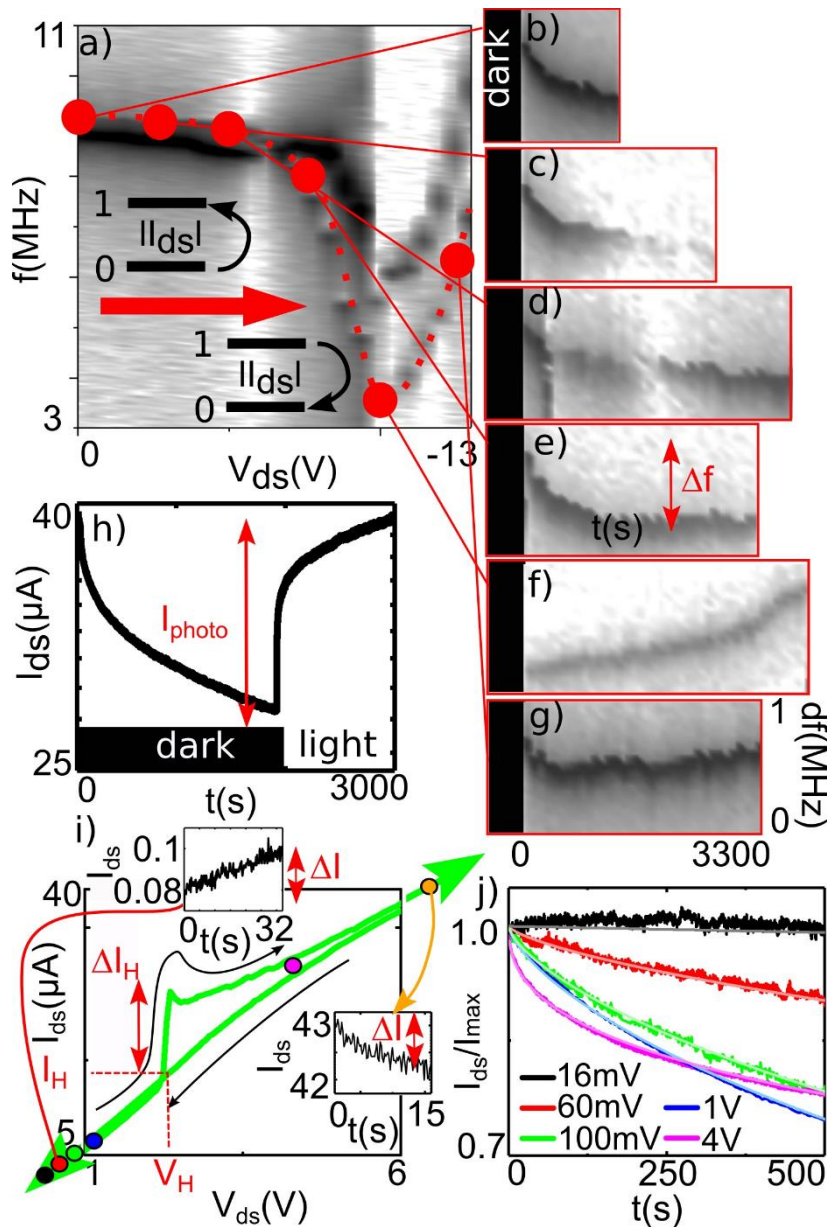


Figure 4 Correlation between the current and the mechanical frequency. In a, we traced the optomechanical response of our system for the fundamental mode of two adjacent resonators, with V_{ds} increasing (the reverse sweeping was in SI). We observed a softening of the mechanical resonance mode from 9.2 to 3.4 MHz. From b to g, the temporal evolution of the mechanical response was measured at different values of V_{ds} . The resonant mode slowly decreased for about 400-500s, by Δf , for $V_{ds} < V_H$ and tended to increase for the higher values $V_{ds} > V_H$. This dynamic was strongly correlated with the current properties of our sample. h) The slow time evolution of the current I_{ds} which decreased by I_{photo} in the dark and increased under the laser light, with $V_{ds} > V_H$ i) A zoom of the $I_{ds}(V_{ds})$ curve of Figure 2 around the memristive charge accumulation represented by a current step ΔI_H at a threshold position (V_H, I_H). In the two insets, for both regimes, at a fixed V_{ds} value above and below V_H , the evolution during the first tens of seconds of the current when the light was already ON. Below the V_H threshold, I_{ds} increased by ΔI and above V_H , I_{ds} decreased in strong analogy with the $-\Delta f$ dependence described in (a-e) and (f-g). After almost 100s, the current tended to increase again in both cases due to I_{photo} , in accordance with (h). j) Time relaxation of the normalized photocurrent at different V_{ds} with respective exponential decay fit

In Figures 4a-g, as for the PPC, we have identified long-lasting dynamics for S_V defects *via* nanomechanical measurements. They are also correlated to memristive effect. After keeping our device in the dark for 30 minutes, we switched ON the laser onto our sample and immediately measured the vibration and its temporal evolution at different values of V_{ds} . Surprisingly, at low voltages, the mechanical frequency downshifted by $\Delta f = 0.3-0.8$ MHz over a long period of time. This is similar to the PPC with typical timescale close to $\tau \sim 400-500$ s and a modification at V_H and above; the evolution of Δf at long delays corresponds this time to a strong hardening of MoS_2 . We point out the strong analogy between Δf and ΔI , and their relation to the memristive effect, Δf being without significant parasitic contributions. This slow effect seems intrinsically different from the fast memristive effect observed in $I-V$ in Figure 2 and to the phase transition of MoS_2 but related to it. We believe this antagonism lies in their common point; the S_V vacancies. Indeed, for the same S_V diffusion in L^2/τ , we can have completely different dynamic τ if we consider different length L as the sample length in micrometer and a local, nanometric, effect. PPC and memristive effect are simply two different consequences of S_V diffusion over different scales.

All the above-mentioned results link the memristive effect, induced by a phase transition, to the diffusion of the S_V defects over a nanometric length. From literature, the relation between S_V and the 2H-1T' phase transition first lies in the capacity of S_V centers to agglomerate in lines, referred as S_V clusters, or in an intermediate S-poor α -phase^{8,31}. Additionally, dynamics of the defective centers can also play a role, as a line of vacancies can release the strong repulsion at the 2H-1T' interface (from a 2H phase to a 1T phase, S atoms are sliding together on one side of the 2D material). The dynamics of S_V clustering and subsequent local 1T' phase transition are examined here using first-principles calculations. Figures 5a and 5b represent the S_V diffusion pathway and the corresponding barrier. We find that in the electronic ground state, the diffusion barrier is quite high (2.3 eV), and S_V is thus an immobile species. When the electron is excited by laser irradiation, the diffusion barrier is reduced to 1.04 eV and the S_V diffusion is facilitated.

Such a S_V diffusion can lead to a vacancy clustering.^{36,37} Using a rate equation, one can quantitatively understand the dynamics of S_V clustering. We consider three processes: (1) the diffusion of a single S vacancy ($1Sv$), (2) the vacancy clustering [$1Sv + nSv \rightarrow (n+1)Sv$], and (3) the dissociation of a vacancy cluster [$nSv \rightarrow 1Sv + (n-1)Sv$]. Here, nSv denotes the n S vacancy cluster. The time variation of the nSv concentration, denoted as $[nSv]$, is calculated using the following coupled equations:

$$\frac{d[1Sv]}{dt} = -k_o[1Sv][1Sv] - \sum_{n=1} k_o[1Sv][nSv] + k_d(2Sv)[2Sv] + \sum_{n=2} k_d(nSv)[nSv]$$

$$\frac{d[nSv]}{dt} = k_o[1Sv][(n-1)Sv] - k_o[1Sv][nSv] + k_d((n+1)Sv)[(n+1)Sv] - k_d(nSv)[nSv], \text{ for } n \geq 2$$

Because the ordering is determined by the diffusion $1Sv$, the clustering rate k_o can be calculated by

$$k_o = 2\pi a^2 f \exp\left[\frac{-E_{diff}}{k_B T}\right] / \ln\left[\frac{1}{a\sqrt{\pi}[1Sv]}\right].$$

Here, E_{diff} is the diffusion energy barrier of 1Sv, a is the MoS₂ lattice constant, and f is the vibrational frequency.³⁸ The dissociation rate is $k_d = f \exp[-E_{dis}(nSv)/k_B T]$, where $E_{dis}(nSv)$ is the dissociation energy barrier, given by the summation of E_{diff} and the binding energy between 1Sv and (n-1)Sv.^{36,39} We use the calculated binding energies for the di-, tri-, and tetravacancy, that is, 0.08, 0.19, and 0.25 eV,¹¹ respectively, but set to 0.30 eV for the binding energies of larger vacancy clusters.

As an initial condition, we set $[1Sv] = 2.0 \times 10^{13} \text{ cm}^{-2}$, which corresponds to 1% 1Sv vacancies, and $[nSv] = 0$ for $n \geq 2$. Figure 5c shows that, in the electronic ground state, no vacancy clustering is found until 0.1 s, because of the low diffusivity of 1Sv. On the other hand, Figure 5e shows that, in the electronic excited state, the enhanced diffusivity of 1Sv leads to large vacancy clustering. Such a vacancy cluster nSv , is associated to a local 1T' phase within an area of $A = \sqrt{3}/4 \cdot (na)^2$.³⁷ (see Figure 5c). Thus, the ratio of the total area of the 1T' phase $A_{1T'}$ to the area of the sample A_{sample} is given by

$$A_{1T'}/A_{sample} = \frac{\sqrt{3}}{4} \sum_{n=2} [nSv](na)^2.$$

Using these reaction rates, we show in Figure 5f that approximately 5% of the 2H MoS₂ area can transition to the 1T' phase within 100 ms.

Under simulation, we have established, under laser illumination, a strong reduction of the barrier energy for diffusion of vacancies, from 2.3 eV to 1.04 eV and the enhancement of Sv clustering when the density is only 1% in the material. It is in accordance with experimental results showing E is reduced even further, to 0.5 to 0.8 eV, when the Sv concentration is higher^{35,40,41} and closer to the 18% in our MoS₂. The 1T' phase was observed after the incorporation of S vacancies in ref.³¹

We also confirm the trace of few percent of the 1T' phase in our sample through Raman and photoemission spectroscopy (see Supplementary Information Figure S9). During the voltage sweeping, the S vacancies tend to conglomerate in clusters or lines rather than be spread out when subjected to an electronic potential^{8,11} and form, in a reversible way, the boundary precursor of the 1T phase. Along the measurement, we modulated experimentally by only 1% the density of 1T' phase but it is enough to induce the memristive effect and the mechanical softening. We show that the control over Sv diffusion is a substitute to usual doping method inducing a phase transition and fully tunable in real devices.

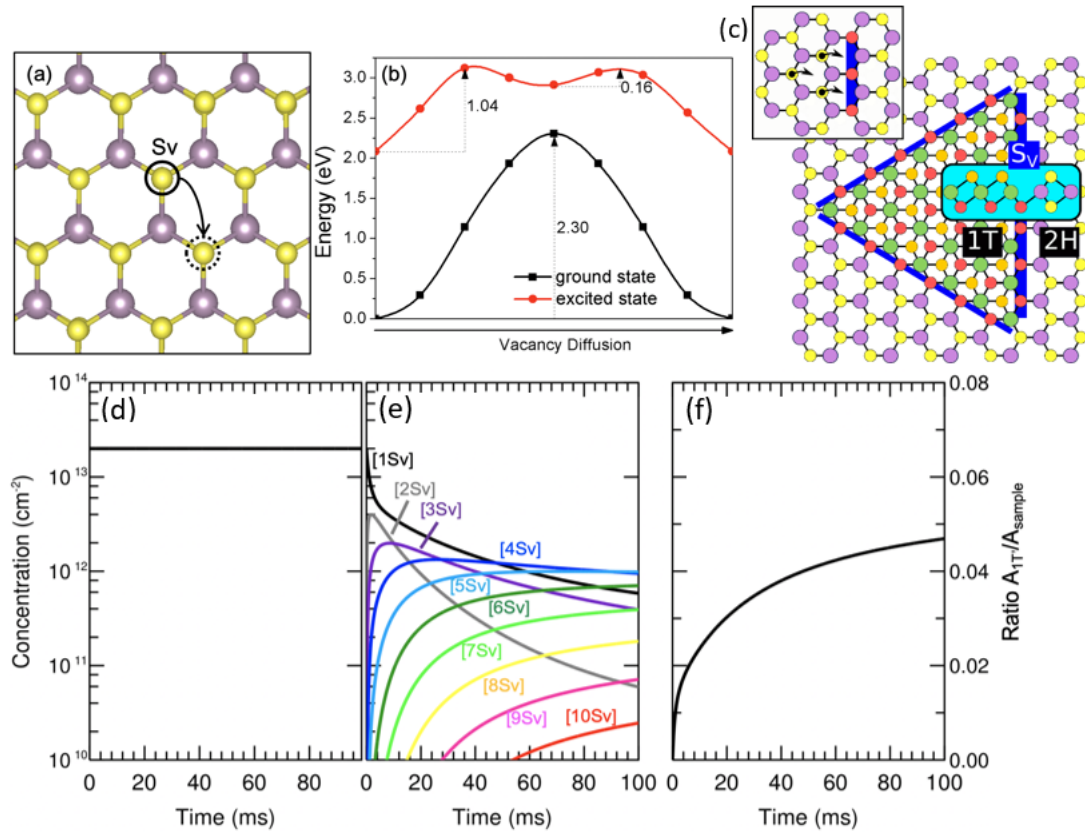


Figure 5 (a) Pathway schematics and (b) energy variation of the 1Sv diffusion. In (b), black and red lines stand for the electronic ground and excited states, respectively. c) Schematic for the formation of a 1T phase triangular shape into the natural 2H phase, due to mainly sulfur displacement, and allowed by the presence, at minima, of boundaries lines of Sulfur vacancies. Time evolution of the concentration of the n vacancy cluster [nSv] in (d) ground and (e) excited states. (f) The change ratio of the total area of the 1T' phase $A_{1T'}$ to the area of the sample A_{sample} by the vacancy clustering in the excited state, *i.e.*, in (e).

To finish the discussion, we comment here about the slow time relaxation of Sv centers ($t = 500s$) for PPC and the voltage dependence. We naively defined the self-diffusion D of Sv centers along the MoS₂ at equilibrium⁴² by: $D = a^2 \cdot k_B T / h \cdot \exp(-E_{diff} / k_B T) 10^{-15} - 10^{-20} m^2 \cdot s^{-1}$. h is the Planck constant and E_{diff} is 0.5 to 0.8 eV.^{35,40,41} Another way to define D is $D \sim L^2 / \tau \sim 10^{-15} m^2 \cdot s^{-1}$ with the typical length of our samples, $L = 1 \mu m$. It is in total agreement with reported values of $D = 3,8 \cdot 10^{-22} m^2 \cdot s^{-1}$ ($D = 5 \cdot 10^{-19} m^2 \cdot s^{-1}$) under electron irradiation.^{35,40} PPC and phase transition are related to Sv diffusion, the difference is the locality of the latter with length around ~ 1 nm; the dynamic is therefore 6 order of magnitude faster for the transition and the memristive effect. When an electrical potential is applied, the Nernst-Einstein law define an equilibrium where the Sv current compensate the diffusion. This relation defines an Sv drift speed $v = De / k_B T \cdot V_{ds} / \Delta L$ of 10 nm/s at $V_{ds} = V_H \sim 2.5V$, which is favorable for a quick and local clustering of vacancies expected in the phase transition. Here, $\Delta L \approx 10 \mu m$ is the electrode distance and e is the elementary charge.

Conclusion

To conclude, we have demonstrated the relation between memristive effects in a monocrystalline MoS₂ device of monolayer thickness and an intrinsic crystal phase 2H-1T'

transition using a simple yet effective optoelectromechanical technique. As mechanical vibrations are extremely sensitive to strain (ultimately $\Delta e \sim 10^{-10}$ with $\Delta f/f \sim 10^{-6}$),⁴³ our method is non-disturbing, local and compatible with other *in situ* electronic and optoelectronic measurements. The S_V diffusion was found to play a key role in the phase transition, which was evidenced *via* the slow dynamics of both PPCs and nanomechanical vibrations. Additionally, theoretical calculations prove that a high reduction in the energy barrier of S_V diffusion is important to yield the phase transition, due to S_V clustering under laser irradiation. Suspended single layer MoS₂ with a high S_V concentration is therefore a promising and low-cost system for future applications, in particular in the electrochemical hydrogen production. Controlling the diffusion of the S_V defects appears to be the main tool to exploit all properties of MoS₂, as well as other 2D TMDs.

Experimental section;

Fabrication method

For the sample fabrication, we embedded a large interdigitated gold metallic contact, 50nm, in a Si/SiO₂ substrate by dry etching and e-beam lithography in order for the top of the contact to be at the same level as the substrate surface. The square array of pillars (pitch 1 micron) was created by dry etching of the SiO₂, with an evaporated hard Ni mask (70nm). A PMMA resist was spin-coated onto the as-grown MoS₂ flakes resting on the SiO₂ substrate using during CVD growth.^{44,45} Large monocrystalline flake of monolayer MoS₂, together with the resist layer, were detached from the growth substrate by wet etching in a KOH solution and rinsed in deionized water. Still in the water, the PMMA layer containing the MoS₂ flakes layer was deposited on the array of pillars between the electrical contacts. The resist was then removed with acetone and the sample was finally dried with a critical point dryer.

Experiment

Electrostatic gating was provided by the doped Si substrate. For the measurement, we used a capacitive excitation and an optomechanical detection according to ref.²⁵ We measured the reflected signal of a laser (633nm, $\sim 10\mu\text{W}$) with both a Michelson interferometer and *in situ* Fabry-Perot cavities formed by the space between the substrate and the MoS₂. All the measurements were performed at ambient temperature under vacuum. The vibration responsivity of the optical cavity MoS₂-substrate had been optimized for enhanced reflectance (see supplementary information).

Calculation method:

The first principle calculations were performed using density functional theory⁴⁶ with the projected augmented wave formalism⁴⁷ as implemented in the Vienna *ab initio* simulation package. The exchange and correlation effects were described by the Perdew–Burke–Ernzerhof version of the generalized gradient approximation.⁴⁸ An energy cutoff of 400 eV was set for the plane wave expansion. We used a 5×5 supercell of monolayer MoS₂ with a single vacancy to simulate the vacancy diffusion in MoS₂. A 15 Å thick vacuum layer was included to avoid the interaction between the periodic slabs. To mimic the electronic excitation, we performed occupation-constrained DFT calculations^{49,50} in which we removed electrons from the highest occupied band and placed them at the lowest unoccupied band. In addition, we assume the elevated temperature $T = 300\text{ °C}$ by the laser irradiation (see supplementary information).

Acknowledgments: We thanks Fabrice Oehler for his comments. Experimental work was supported by French grants ANR ANETHUM (ANR-19-CE24-0021) and ANR Deus-nano (ANR-19-CE42-0005), by the European Union’s Horizon 2020 research and innovation program under grant agreement No 732894 (FET Proactive HOT) and by the French Renatech

network. M.Q.Z. and A.T.C.J. acknowledges support from the Chinese/U.S. National Science Foundation EAGER 1838412 and MRSEC DMR-1720530. First-principles calculation was supported by National Natural Science Foundation of China (11874019) (C.S), Chinese/U.S. National Research Council of Science & Technology (No. CAP-18-05-KAERI) (J.B.), and U.S. Department of Energy (DOE) under Grant No. DESC0002623 (S.B.Z.).

Supplementary information: Additional information is available online. The Supplementary Information proposes additional measurements on memristive effect and PPC with some models. It also details a description of the movement equation of the resonator as well as a more complete discussion on the origin of the observed mechanical softening.

Author contribution: J.C. and A.O. conceived and designed the experiments, M.Q.Z., A.T.C.J., A.D., X.L. and J.C. designed and fabricated the devices, I.H., L.K. and J.C. performed the experiments, Q.Z., S.Z., J.B. developed the theory, and J.B., J.C., L.K., A.O. co-wrote the paper. All the authors discussed the results and commented on the manuscript.

References;

- (1) Liu, Y.; Guo, J.; Wu, Y.; Zhu, E.; Weiss, N. O.; He, Q.; Wu, H.; Cheng, H.-C.; Xu, Y.; Shakir, I.; Huang, Y.; Duan, X. Pushing the Performance Limit of Sub-100 Nm Molybdenum Disulfide Transistors. *Nano Lett.* **2016**, *16*, 6337–6342.
- (2) Sarkar, D.; Xie, X.; Liu, W.; Cao, W.; Kang, J.; Gong, Y.; Kraemer, S.; Ajayan, P. M.; Banerjee, K. A Subthermionic Tunnel Field-Effect Transistor with an Atomically Thin Channel. *Nature* **2015**, *526*, 91–95.
- (3) Mak, K. F.; He, K.; Lee, C.; Lee, G. H.; Hone, J.; Heinz, T. F.; Shan, J. Tightly Bound Trions in Monolayer MoS₂. *Nat. Mater.* **2013**, *12*, 207–211.
- (4) Zribi, J.; Khalil, L.; Zheng, B.; Avila, J.; Pierucci, D.; Brulé, T.; Chaste, J.; Lhuillier, E.; Asensio, M. C.; Pan, A.; Ouerghi, A. Strong Interlayer Hybridization in the Aligned SnS₂/WSe₂ Hetero-Bilayer Structure. *Npj 2D Mater. Appl.* **2019**, *3*, 1–7.
- (5) Li, H.; Contryman, A. W.; Qian, X.; Ardakani, S. M.; Gong, Y.; Wang, X.; Weisse, J. M.; Lee, C. H.; Zhao, J.; Ajayan, P. M.; Li, J.; Manoharan, H. C.; Zheng, X. Optoelectronic Crystal of Artificial Atoms in Strain-Textured Molybdenum Disulfide. *Nat. Commun.* **2015**, *6*, 7381.
- (6) Sangwan, V. K.; Jariwala, D.; Kim, I. S.; Chen, K.-S.; Marks, T. J.; Lauhon, L. J.; Hersam, M. C. Gate-Tunable Memristive Phenomena Mediated by Grain Boundaries in Single-Layer MoS₂. *Nat. Nanotechnol.* **2015**, *10*, 403–406.
- (7) Yoshida, M.; Suzuki, R.; Zhang, Y.; Nakano, M.; Iwasa, Y. Memristive Phase Switching in Two-Dimensional 1T-TaS₂ Crystals. *Sci. Adv.* **2015**, *1*, e1500606.
- (8) Lin, Y.-C.; Dumcenco, D. O.; Huang, Y.-S.; Suenaga, K. Atomic Mechanism of the Semiconducting-to-Metallic Phase Transition in Single-Layered MoS₂. *Nat. Nanotechnol.* **2014**, *9*, 391–396.
- (9) Cheng, P.; Sun, K.; Hu, Y. H. Memristive Behavior and Ideal Memristor of 1T Phase MoS₂ Nanosheets. *Nano Lett.* **2016**, *16*, 572–576.
- (10) Duerloo, K.-A. N.; Li, Y.; Reed, E. J. Structural Phase Transitions in Two-Dimensional Mo- and W-Dichalcogenide Monolayers. *Nat. Commun.* **2014**, *5*, 4214.
- (11) Le, D.; Rawal, T. B.; Rahman, T. S. Single-Layer MoS₂ with Sulfur Vacancies: Structure and Catalytic Application. *J. Phys. Chem. C* **2014**, *118*, 5346–5351.
- (12) Strukov, D. B.; Snider, G. S.; Stewart, D. R.; Williams, R. S. The Missing Memristor Found. *Nature* **2008**, *453*, 80–83.

- (13) Zhu, X.; Li, D.; Liang, X.; Lu, W. D. Ionic Modulation and Ionic Coupling Effects in MoS₂ Devices for Neuromorphic Computing. *Nat. Mater.* **2019**, *18*, 141–148.
- (14) Li, Y.; Duerloo, K.-A. N.; Wauson, K.; Reed, E. J. Structural Semiconductor-to-Semimetal Phase Transition in Two-Dimensional Materials Induced by Electrostatic Gating. *Nat. Commun.* **2016**, *7*, 10671.
- (15) Ge, R.; Wu, X.; Kim, M.; Shi, J.; Sonde, S.; Tao, L.; Zhang, Y.; Lee, J. C.; Akinwande, D. Atomristor: Nonvolatile Resistance Switching in Atomic Sheets of Transition Metal Dichalcogenides. *Nano Lett.* **2018**, *18*, 434–441.
- (16) Zhang, K.; Cao, Z.-Y.; Chen, X.-J. Effects of Charge-Density-Wave Phase Transition on Electrical Transport and Raman Spectra in 2H-Tantalum Disulfide. *Appl. Phys. Lett.* **2019**, *114*, 141901.
- (17) Eda, G.; Fujita, T.; Yamaguchi, H.; Voiry, D.; Chen, M.; Chhowalla, M. Coherent Atomic and Electronic Heterostructures of Single-Layer MoS₂. *ACS Nano* **2012**, *6*, 7311–7317.
- (18) Papadopoulos, N.; Island, J. O.; Zant, H. S. J. van der; Steele, G. A. Investigating Laser-Induced Phase Engineering in MoS₂ Transistors. *IEEE Trans. Electron Devices* **2018**, *65*, 4053–4058.
- (19) Chaste, J.; Eichler, A.; Moser, J.; Ceballos, G.; Rurali, R.; Bachtold, A. A Nanomechanical Mass Sensor with Yoctogram Resolution. *Nat. Nanotechnol.* **2012**, *7*, 301–304.
- (20) Bunch, J. S.; Zande, A. M. van der; Verbridge, S. S.; Frank, I. W.; Tanenbaum, D. M.; Parpia, J. M.; Craighead, H. G.; McEuen, P. L. Electromechanical Resonators from Graphene Sheets. *Science* **2007**, *315*, 490–493.
- (21) Blees, M. K.; Barnard, A. W.; Rose, P. A.; Roberts, S. P.; McGill, K. L.; Huang, P. Y.; Ruyack, A. R.; Kevek, J. W.; Kobrin, B.; Muller, D. A.; McEuen, P. L. Graphene Kirigami. *Nature* **2015**, *524*, 204–207.
- (22) Eichler, A.; Moser, J.; Chaste, J.; Zdrojek, M.; Wilson-Rae, I.; Bachtold, A. Nonlinear Damping in Mechanical Resonators Made from Carbon Nanotubes and Graphene. *Nat. Nanotechnol.* **2011**, *6*, 339–342.
- (23) Liu, C.-H.; Kim, I. S.; Lauhon, L. J. Optical Control of Mechanical Mode-Coupling within a MoS₂ Resonator in the Strong-Coupling Regime. *Nano Lett.* **2015**, *15*, 6727–6731.
- (24) Lee, J.; Wang, Z.; He, K.; Shan, J.; Feng, P. X.-L. High Frequency MoS₂ Nanomechanical Resonators. *ACS Nano* **2013**, *7*, 6086–6091.
- (25) Morell, N.; Reserbat-Plantey, A.; Tsioutsios, I.; Schädler, K. G.; Dubin, F.; Koppens, F. H. L.; Bachtold, A. High Quality Factor Mechanical Resonators Based on WSe₂ Monolayers. *Nano Lett.* **2016**, *16*, 5102–5108.
- (26) Manzeli, S.; Dumcenco, D.; Migliato Marega, G.; Kis, A. Self-Sensing, Tunable Monolayer MoS₂ Nanoelectromechanical Resonators. *Nat. Commun.* **2019**, *10*, 4831.
- (27) Pierucci, D.; Henck, H.; Ben Aziza, Z.; Naylor, C. H.; Balan, A.; Rault, J. E.; Silly, M. G.; Dappe, Y. J.; Bertran, F.; Le Fèvre, P.; Sirotti, F.; Johnson Jr, A. T. C.; Ouerghi, A. Tunable Doping in Hydrogenated Single Layered Molybdenum Disulfide. *ACS Nano* **2017**, *11*, 1755–1761.
- (28) Naylor, C. H.; Kybert, N. J.; Schneier, C.; Xi, J.; Romero, G.; Saven, J. G.; Liu, R.; Johnson, A. T. C. Scalable Production of Molybdenum Disulfide Based Biosensors. *ACS Nano* **2016**, *10*, 6173–6179.
- (29) Chaste, J.; Missaoui, A.; Huang, S.; Henck, H.; Ben Aziza, Z.; Ferlazzo, L.; Naylor, C.; Balan, A.; Johnson Jr, A. T. C.; Braive, R.; Ouerghi, A. Intrinsic Properties of Suspended MoS₂ on SiO₂/Si Pillar Arrays for Nanomechanics and Optics. *ACS Nano* **2018**, *12*, 3235–3242.

- (30) Furchi, M. M.; Polyushkin, D. K.; Pospischil, A.; Mueller, T. Mechanisms of Photoconductivity in Atomically Thin MoS₂. *Nano Lett.* **2014**, *14*, 6165–6170.
- (31) Gan, X.; Lee, L. Y. S.; Wong, K.; Lo, T. W.; Ho, K. H.; Lei, D. Y.; Zhao, H. 2H/1T Phase Transition of Multilayer MoS₂ by Electrochemical Incorporation of S Vacancies. *ACS Appl. Energy Mater.* **2018**, *1*, 4754–4765.
- (32) Sangwan, V. K.; Lee, H.-S.; Bergeron, H.; Balla, I.; Beck, M. E.; Chen, K.-S.; Hersam, M. C. Multi-Terminal Memtransistors from Polycrystalline Monolayer Molybdenum Disulfide. *Nature* **2018**, *554*, 500–504.
- (33) Di Bartolomeo, A.; Genovese, L.; Foller, T.; Giubileo, F.; Luongo, G.; Croin, L.; Liang, S.-J.; Ang, L. K.; Schleberger, M. Electrical Transport and Persistent Photoconductivity in Monolayer MoS₂ Phototransistors. *Nanotechnology* **2017**, *28*, 214002.
- (34) Wu, Y.-C.; Liu, C.-H.; Chen, S.-Y.; Shih, F.-Y.; Ho, P.-H.; Chen, C.-W.; Liang, C.-T.; Wang, W.-H. Extrinsic Origin of Persistent Photoconductivity in Monolayer MoS₂ Field Effect Transistors. *Sci. Rep.* **2015**, *5*.
- (35) Komsa, H.-P.; Kurasch, S.; Lehtinen, O.; Kaiser, U.; Krasheninnikov, A. V. From Point to Extended Defects in Two-Dimensional MoS₂: Evolution of Atomic Structure under Electron Irradiation. *Phys. Rev. B* **2013**, *88*, 035301.
- (36) Bang, J.; Kim, Y.-S.; Park, C. H.; Gao, F.; Zhang, S. B. Understanding the Presence of Vacancy Clusters in ZnO from a Kinetic Perspective. *Appl. Phys. Lett.* **2014**, *104*, 252101.
- (37) Si, C.; Choe, D.; Xie, W.; Wang, H.; Sun, Z.; Bang, J.; Zhang, S. Photoinduced Vacancy Ordering and Phase Transition in MoTe₂. *Nano Lett.* **2019**, *19*, 3612–3617.
- (38) Hardt, S. L. Rates of Diffusion Controlled Reactions in One, Two and Three Dimensions. *Biophys. Chem.* **1979**, *10*, 239–243.
- (39) Fahey, P. M.; Griffin, P. B.; Plummer, J. D. Point Defects and Dopant Diffusion in Silicon. *Rev. Mod. Phys.* **1989**, *61*, 289–384.
- (40) Precner, M.; Polaković, T.; Qiao, Q.; Trainer, D. J.; Putilov, A. V.; Giorgio, C. D.; Cone, I.; Zhu, Y.; Xi, X. X.; Iavarone, M.; Karapetrov, G. Evolution of Metastable Defects and Its Effect on the Electronic Properties of MoS₂ Films. *Sci. Rep.* **2018**, *8*, 6724.
- (41) Zou, X.; Liu, M.; Shi, Z.; Yakobson, B. I. Environment-Controlled Dislocation Migration and Superplasticity in Monolayer MoS₂. *Nano Lett.* **2015**, *15*, 3495–3500.
- (42) Zhang, Y. N.; Law, M.; Wu, R. Q. Atomistic Modeling of Sulfur Vacancy Diffusion Near Iron Pyrite Surfaces. *J. Phys. Chem. C* **2015**, *119*, 24859–24864.
- (43) Sansa, M.; Sage, E.; Bullard, E. C.; Gély, M.; Alava, T.; Colinet, E.; Naik, A. K.; Villanueva, L. G.; Duraffourg, L.; Roukes, M. L.; Jourdan, G.; Hentz, S. Frequency Fluctuations in Silicon Nanoresonators. *Nat. Nanotechnol.* **2016**, *11*, 552–558.
- (44) Henck, H.; Pierucci, D.; Chaste, J.; Naylor, C. H.; Avila, J.; Balan, A.; Silly, M. G.; Asensio, M. C.; Sirotti, F.; Johnson, A. T. C.; Lhuillier, E.; Ouerghi, A. Electrolytic Phototransistor Based on Graphene-MoS₂ van der Waals *p-n* Heterojunction with Tunable Photoresponse. *Appl. Phys. Lett.* **2016**, *109*, 113103.
- (45) Pierucci, D.; Henck, H.; Avila, J.; Balan, A.; Naylor, C. H.; Patriarche, G.; Dappe, Y. J.; Silly, M. G.; Sirotti, F.; Johnson, A. T. C.; Asensio, M. C.; Ouerghi, A. Band Alignment and Minigaps in Monolayer MoS₂-Graphene van der Waals Heterostructures. *Nano Lett.* **2016**, *16*, 4054–4061.
- (46) Kresse, G.; Furthmüller, J. Efficient Iterative Schemes for *Ab Initio* Total-Energy Calculations Using a Plane-Wave Basis Set. *Phys. Rev. B* **1996**, *54*, 11169–11186.
- (47) Kresse, G.; Joubert, D. From ultrasoft pseudopotentials to the projector augmented-wave method. *Phys. Rev. B* **1999**, *59*, 1758–1775.

- (48) Perdew, J. P.; Burke, K.; Ernzerhof, M. Generalized Gradient Approximation Made Simple. *Phys. Rev. Lett.* **1996**, *77*, 3865–3868.
- (49) Bang, J.; Wang, Z.; Gao, F.; Meng, S.; Zhang, S. B. Suppression of Nonradiative Recombination in Ionic Insulators by Defects: Role of Fast Electron Trapping in Tl-Doped CsI. *Phys. Rev. B* **2013**, *87*, 205206.
- (50) Bang, J.; Sun, Y. Y.; Song, J.-H.; Zhang, S. B. Carrier-Induced Transient Defect Mechanism for Non-Radiative Recombination in InGaN Light-Emitting Devices. *Sci. Rep.* **2016**, *6*, 1–6.

Supplementary information for:

Phase Transition in a Memristive Suspended MoS₂ Monolayer Probed by Opto- and Electro-Mechanics.

Julien Chaste^{1*}, Imen Hnid¹, Chen Si², Lama Khalil¹, Alan Durnez¹, Xavier Lafosse¹, Meng-Qiang Zhao³, A.T. Charlie Johnson³, Shengbai Zhang⁴, Junhyeok Bang^{5**}, Abdelkarim Ouerghi¹

¹ Université Paris-Saclay, CNRS, Centre de Nanosciences et de Nanotechnologies, 91120, Palaiseau, France.

² School of Materials Science and Engineering, Beihang University, Beijing 100191, China

³ Department of Physics and Astronomy, University of Pennsylvania, 209S 33rd Street, Philadelphia, Pennsylvania 19104 6396, United States

⁴ Department of Physics, Applied Physics, & Astronomy, Rensselaer Polytechnic Institute, Troy, New York 12180, USA

⁵ Department of Physics, Chungbuk National University, Cheongju 28644, Republic of Korea

* Corresponding author: julien.chaste@universite-paris-saclay.fr

* Corresponding for theory: jbang@cbnu.ac.kr

Table of contents

| | |
|--|----|
| S0: Sample images | 17 |
| S1: Electrical hysteresis and memristivity | 17 |
| S2: Others nanomechanical memristive device..... | 19 |
| S3: Fully clamped drum resonator model | 20 |
| S4: Mechanical hardening and softening | 24 |
| Mass deposition; | 24 |
| Capacitive softening | 25 |
| Heating; | 26 |
| S_v diffusion along the membrane | 27 |
| Membrane slipping | 28 |
| Piezoelectricity | 28 |
| Dielectric force | 28 |
| S5: Relation between the reflectance and the cavity length. | 29 |
| S6: Memristor energy | 29 |
| S7: Persistent current measurements | 30 |
| S8: 1T' phase signature in our MoS ₂ with Raman and photoemission spectroscopy..... | 31 |
| S9: Writing/ erasing processes and 1T' phase evidence in our MoS ₂ | 31 |

S0: Sample images

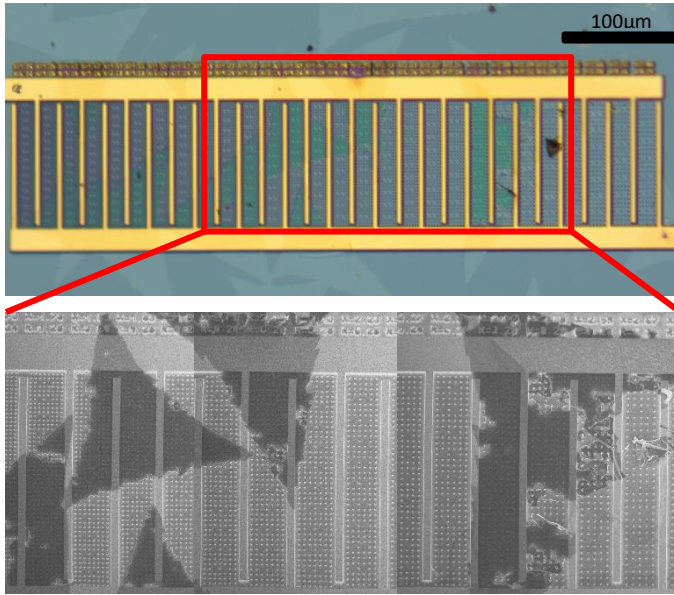


Figure S0; Optical image and E beam image of a typical sample used in this study, most of the MoS₂ flake are suspended over SiO₂ pillars and gold contacts

The MoS₂ sample presented in Figure S0 corresponds to most of the measurements achieved in the paper. One interest of this configuration, with interdigitated contacts is the possibility to optically illuminate one specific area of the sample and subsequently to electrically “activate” this same area due to the strong photocurrent in the sample.

Convex edges and sulfur vacancies

Another indirect consequence or signature of a high density of defect is the peculiar form of the MoS₂ triangle with convex edges. MoS₂ present in Figure S0 has this specific shape. Similar images on our MoS₂ with such type of edge are also observed in the SOI of the reference ¹ and is well describe in reference. ²

S1: Electrical hysteresis and memristivity

We measure the memristive effect in our devices and define the two states 0 and 1, they represent the maximum (minimum) current achievable for each V_{ds} and P . The non-linearity of the $I_{ds}(V_{ds})$ curve is not as strong as previous memristive devices³, even for MoS₂⁴ but is significant. We present, in the Figure S2a, the two current states 0 and 1 and the protocol to pass from state 0 to state 1 and vice versa. We define two inflexion points P^- and P^+ (at $-5.8V$ and $+5.8V$ respectively for the sample in Figure S2a), two erasing area for $V_{ds} > P^+$ and $V_{ds} < P^-$ and a writing area $P^- < V_{ds} < P^+$. Our device is also electrically bipolar: in fact, during a voltage polarity sweep restricted to positive values $+V_{ds}$ (or negative, $-V_{ds}$), the step of the accumulated charge Δq or ΔI_H appears only for the first sweep unless an opposite voltage $-V_{ds}$ ($+V_{ds}$) is applied to the device (see Figure S1c).

In each case, the first cycle shows a current transition from state 0 to 1 at the inflexion point but for the second cycle and above, it is necessary to sweep to the opposite erase area (of opposite sign in V_{ds}) in order to recover the hysteresis effect during a second cycle. If this is not the case, there is no transition in the device and it remains in the 0 state for the rest of the cycles, as shown in the Figure S2b.

Note that the hysteresis position and amplitude remain quite similar when the bias sweep rate is tuned from 20mV/s to 2V/s.

Within our bipolar memristor device, it is possible to block the current in the 0 state or the 1 state by sweeping V_{ds} carefully between the different regions

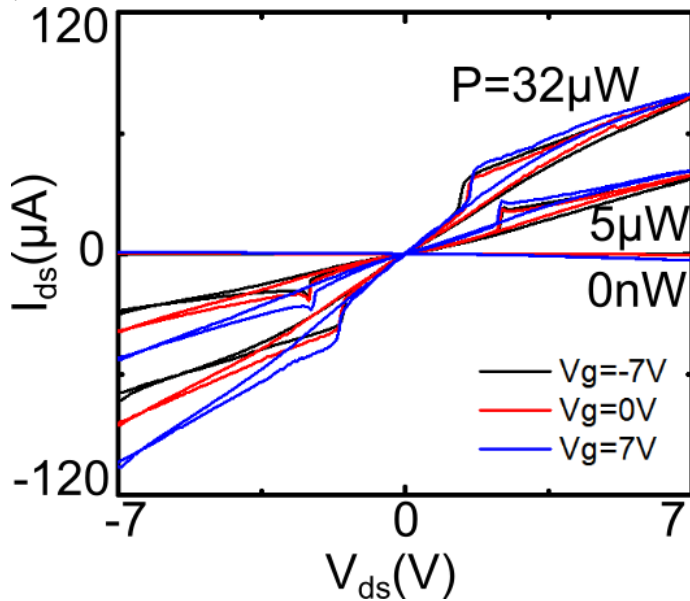


Figure S1a Measure of $I_{ds}(V_{ds})$ for different V_g and laser power. The gate voltage does not induce any notable modification of the hysteresis position or amplitude even if a decrease of the resistance value is seen with higher gate voltage in the current-voltage dependence

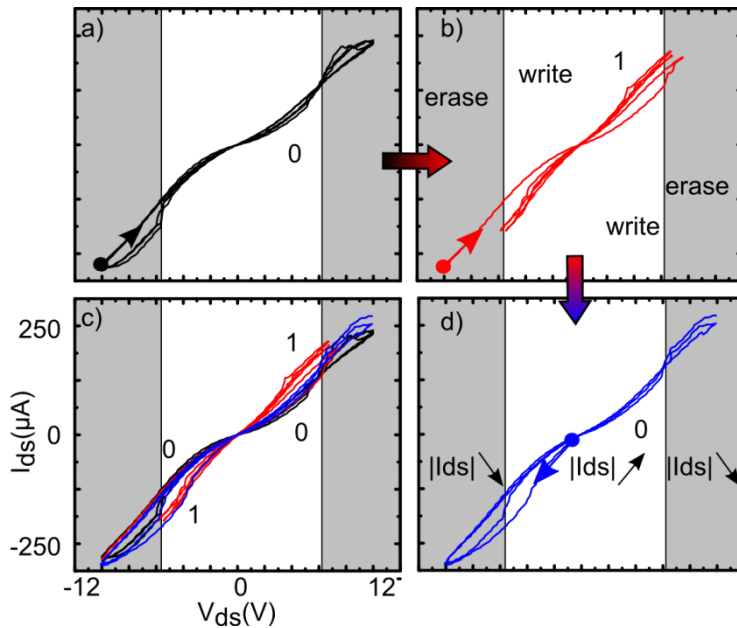


Figure S1b Memory effect in the MoS₂ device with state 0 and 1. a) $I_{ds}(V_{ds})$ curve with a starting point at $V_{ds}=-10V$ and sweep from -10 to 10V. b) $I_{ds}(V_{ds})$ curve with a starting point at $V_{ds}=-10V$ and sweep from -5.8 to 5.8V. d) $I_{ds}(V_{ds})$ curve with a starting point at $V_{ds}=0V$ and sweep from -10 to 10V. d) The three measurements are taken in the order: black then red then blue.

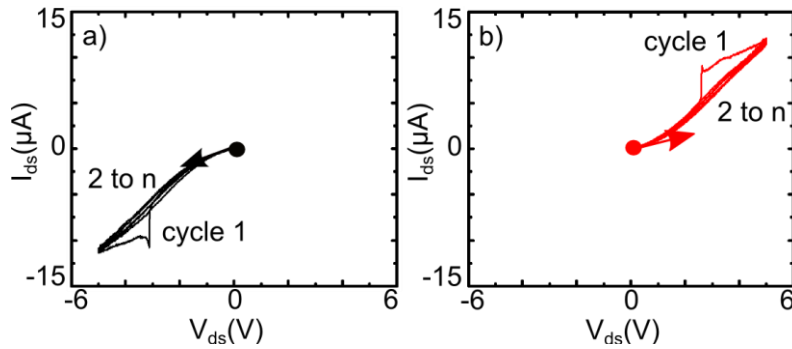


Figure S1c Memory effect for only one cycle when V_{ds} sign does not change. a) $I_{ds}(V_{ds})$ curve with a starting point at $V_{ds}=0V$ and few back and forth sweeps from 0 to -10V. b) $I_{ds}(V_{ds})$ curve with a starting point at $V_{ds}=0V$ and few back and forth sweeps from 0 to 10V.

S2: Others nanomechanical memristive device

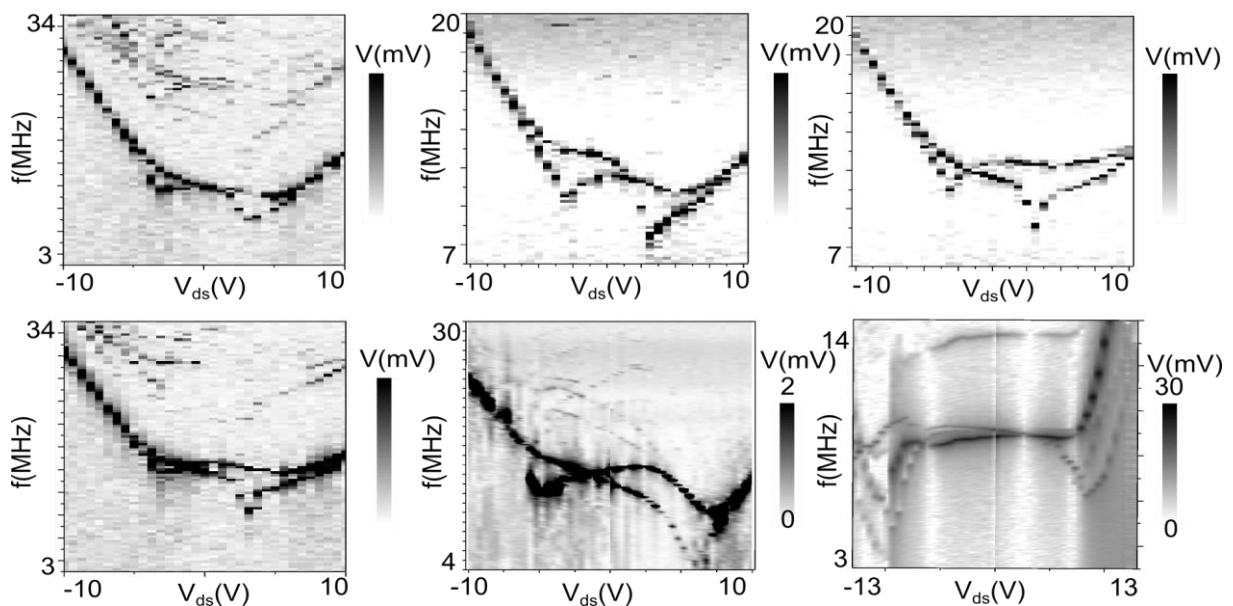


Figure S2a Memory effect for only one cycle when V_{ds} sign does not change. a) $I_{ds}(V_{ds})$ curve with a starting

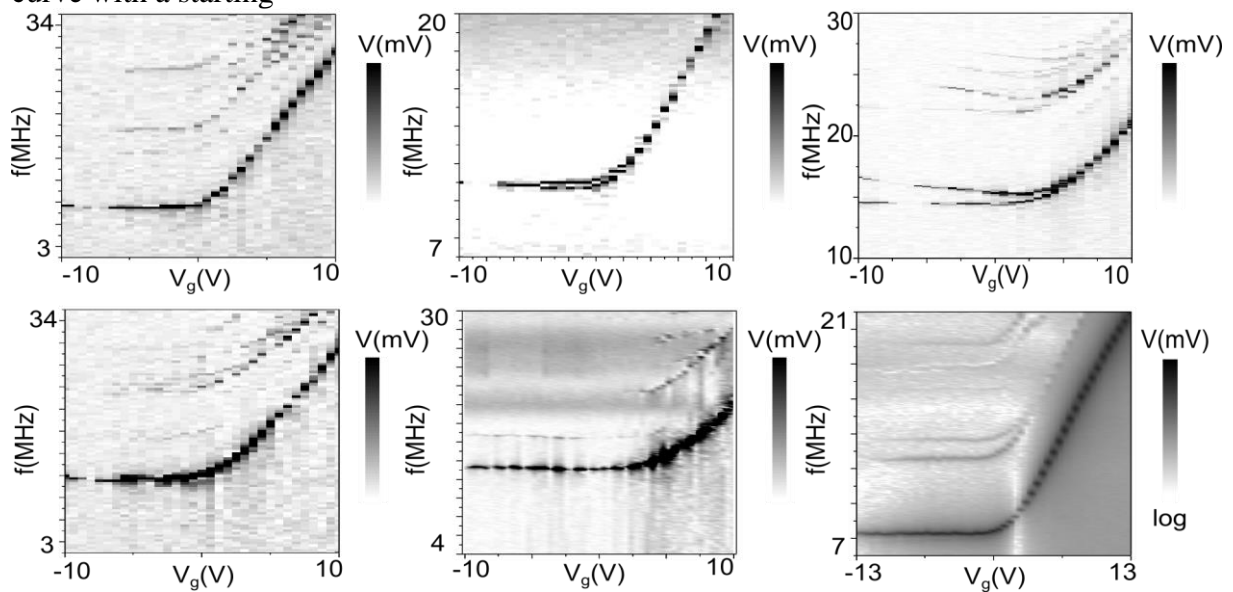


Figure S2b Memory effect for only one cycle when V_{ds} sign does not change. a) $I_{ds}(V_{ds})$ curve with a starting

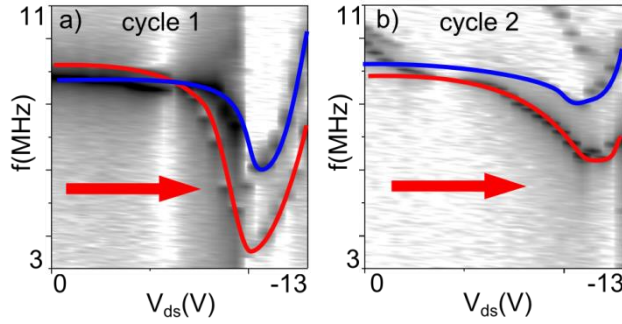


Figure S2c Memory effect for only one cycle when V_{ds} sign does not change. a) $I_{ds}(V_{ds})$ curve with a starting

S3: Fully clamped drum resonator model

5–10

Static deflection of a circular membrane

Considering a very thin plate, fully clamped, we work in the membrane limit and neglect the flexural rigidity of our 2D resonator. In circular coordinate, the static shape $w(r)$ of a doubly clamped drum resonator is assumed to be a parabolic shape;

$$w(r) = z \left(1 - \frac{r^2}{R^2} \right) \quad (2)$$

With z the deflection at $r=0$ and R the radius of the membrane

The elastic energy U_{el} is the sum of the bending energy U_b and of the restoring potential energy U_T which comes from its tension. In our case, we have already demonstrated our membrane to be in the tension limit. We only considered the strain energy per unit volume, defined as ^{8,11,12};

$$dU_{el} \approx dU_T = \sum_{i=r,\theta} \sum_{j=r,\theta} \sigma_{ij} \varepsilon_{ij} dV \quad (3)$$

The approximation with a drum has a central symmetry. We consider w the lateral deflection, u the radial displacement and $\varepsilon_{r,\theta}$ the radial and angular strain and we can write

$$\begin{aligned} \varepsilon_{rr}(r) dr &= \varepsilon_r(r) dr = \frac{\partial u}{\partial r} \cdot dr + \frac{1}{2} \left(\frac{\partial w}{\partial r} \right)^2 \cdot dr \text{ and } \varepsilon_{\theta\theta}(r) = \varepsilon_\theta \\ &= \frac{u}{r} \text{ and } \varepsilon_{r\theta} = 0 \end{aligned} \quad (4)$$

Here, $\partial u / \partial r$ is the radial elongation. In our case we replace this term by the initial radial strain-stress duo $\varepsilon_0 - \sigma_0$ which is consider to be uniform along the sample. $2\pi R \cdot \varepsilon_0 = \iint \varepsilon_0 r dr d\theta$. From

Hooke's law, if the tangential strain is assumed to be 0, then we have $\sigma_r - \sigma_\theta = \frac{Et}{(1-\nu^2)} \varepsilon_r$ with ν the Poisson's ratio and E the Young Modulus. Finally, it gives;

$$U_{el} = \frac{1}{2} \frac{Et}{(1-\nu^2)} \int_0^{2\pi} \int_0^R \left(\varepsilon_0 + \frac{1}{2} \left(\frac{\partial w}{\partial r} \right)^2 \right)^2 r dr d\theta \quad (5)$$

In other terms;

$$U_{el} = \frac{2\pi Et z^4}{3(1-\nu^2)R^2} + \frac{\pi E \varepsilon_0 t z^2}{(1-\nu^2)} + \frac{\pi Et \varepsilon_0^2 R^2}{2(1-\nu^2)} \quad (6)$$

$$U_{el} = \frac{\pi Et}{(1-\nu^2)} \cdot \left(\frac{2z^4}{3 \cdot R^2} + \varepsilon_0 z^2 + \frac{\varepsilon_0^2 R^2}{2} \right) \quad (7)$$

$$U_{el} = \frac{\pi Et}{(1-\nu^2)} \cdot z^2 \left(\frac{2z^2}{3 \cdot R^2} + \varepsilon_0 \right) + \frac{\pi Et}{(1-\nu^2)} \cdot \frac{\varepsilon_0^2 R^2}{2} \quad (8)$$

The second term is the initial energy U_{init} resulting from the build-in stress; $U_{init} = 1/2 \int \sigma_0 \varepsilon_0 r dr d\theta$.

If we define the total stress T for a small angle $d\theta$ applied to the membrane as the sum of building stress and the stress due to the deflection of the membrane for the same angle, we have⁸;

$$T(z) = T_0 + T_D(z) = T_0 + \varepsilon_D(z) \frac{Et}{(1-\nu^2)} \quad (9)$$

$$T(z) = T_0 + \frac{Et}{(1-\nu^2)} \frac{1}{R} \int_0^R \frac{1}{2} \cdot \left(\frac{\partial w}{\partial r} \right)^2 dr = T_0 + \frac{2}{3} \frac{Et}{(1-\nu^2)} \frac{z^2}{R^2} \quad (10)$$

If we integrate T over all angle $\int_0^{2\pi} d\theta$, and multiply by $z^2 \cdot t/2$, we retrieve the first term in U_{el} . In other term;

$$U_{el} = \frac{1}{2} \cdot z^2 \cdot 2\pi \cdot T(z) \cdot t + U_{init} \quad (11)$$

This notation will be important for the dynamical description of our membrane.

We want also to noticed that, with similar notation and with a central symmetry, the Bending energy is defined as⁹;

$$U_B = \frac{1}{24} \frac{Et^3}{(1-\nu^2)} \int_0^{2\pi} \int_0^R \left(\frac{\partial^2 w}{\partial r^2} + \frac{1}{r} \frac{\partial w}{\partial r} + \frac{1}{r^2} \frac{\partial^2 w}{\partial \theta^2} \right)^2 r dr d\theta \quad (12)$$

It is also interesting to describe the electrostatic energy $U_C = 1/2 C_g V_g^2$ and develop the capacitance term for small deflection $C_g = C_0 + C'z + C''z^2/2$ where $C' = dC_g/dz$ et $C'' = d^2C_g/dz^2$. Then the electrostatic force is

$$\begin{aligned} U_C &= \frac{1}{2} C_0 V_g^2 + \frac{1}{2} C' z V_g^2 + \frac{1}{4} C'' z^2 V_g^2 = \frac{1}{2} V_g^2 \cdot \epsilon_0 \cdot \iint \left(\frac{1}{d^1} + \frac{w}{d^2} + \frac{w^2}{d^3} \right) r dr d\theta \\ &= \frac{1}{2} \left(\frac{\epsilon_0 \pi R^2}{d^1} \right) V_g^2 + \frac{1}{2} \left(\frac{\epsilon_0 \pi R^2}{2d^2} \right) z V_g^2 + \frac{1}{4} \left(\frac{\epsilon_0 2\pi R^2}{3d^3} \right) z^2 V_g^2 \end{aligned} \quad (13)$$

We can notice the minus sign appearing in the resulting Force $F_C = dU_C/dz = -1/2 dC_g/dz V_g^2$ because we have to apply a fix voltage V_g with an external battery^{13,14} and we must consider the virtual work done on the charging source $U_b = -C_g V_g^2$ to the energy stored in the capacitor. It can also be deduced by derivate the energy, working at constant charge, $U_C = 1/2 q^2/C_g$.

The equilibrium position z is defined by the minimum of energy or $\partial(U_{el} + U_C)/\partial z = 0$

$$\frac{8\pi E t}{3(1-\nu^2)R^2} z^3 + \left(\frac{2\pi E \epsilon_0 t}{(1-\nu^2)} - \frac{1}{2} C'' V_g^2 \right) z - \frac{1}{2} C' V_g^2 = 0 \quad (14)$$

It is a polynomial equation of the form $z^3 + az + b = 0$ with solutions defined by the Cardan method;

$$z = \left((-b - \sqrt{\Delta})/2 \right)^{1/3} + \left((-b + \sqrt{\Delta})/2 \right)^{1/3} \text{ and with } \Delta = b^2 + 4a^3/27 \quad (15)$$

It defined a relation between z and V_g . This equation describes our system only when a deflection z (and w) are no null. It is valid in a regime where the capacitive force V_g is not negligible (high V_g) or when this initial strain itself induced some deflection. At low V_g and in a built-in strain in the plane $\epsilon_r = \partial u/\partial r$, we are in a regime with no deflection ($w=z=0$) and $U_{el} = \pi E t \epsilon_0 R^2/2(1-\nu^2)$. A modification of the built-in strain will not modify the equilibrium position and will not create a deflection. This has to be opposite to a vibration which is an oscillating deflection ($w \neq 0$) and the build-in strain can induce a vibration frequency modification. In other words, a planar modification of the build-in strain can explain our measurements where we obtained a hysterical softening of the vibration and no deflection of the membrane at the same time.

Dynamical deflection of a circular membrane

In this section we will transform $w \rightarrow w + w_{AC}$ and $F_C \rightarrow F_C + F_{AC}$. However, we will also assume $T_M(z)$ and σ_R to be constant because the contribution of a small oscillation around the

equilibrium position to the stress will converge to 0 in a symmetric harmonic potential. It is unambiguous from equation 10 that our system is equivalent to a spring which can vibrate. The main difference consists in the spring constant itself which depend on the deflection amplitude.

The motion equation in this case, is ¹⁰ ;

$$\rho \frac{\partial^2 w}{\partial t^2} = -\kappa \nabla^4 w + T \nabla^2 w + \frac{F_C}{\pi R^2} \quad (16)$$

In polar coordinates, ∇^2 is $\frac{1}{r} \frac{\partial}{\partial r} + \frac{\partial^2}{\partial r^2}$, ρ is the 2D mass density and κ is the bending stiffness. We know the bending term to be negligible in our case¹. As expected, this equation gives the same result for z , T_M and F_C and confirm our description of the harmonic oscillator submitted to a force F_C . Concerning the dynamic counterpart, the mode shape of a circular membrane can be expressed using J_0 , the 0th-order Bessel function of the first kind ¹⁵. Considering the circumference-clamped boundary conditions, the mode shape of the resonance is:

$$w_{AC}(r) = \sum_{n=0}^{\infty} \delta z_n \cdot J_0 \left(\lambda_n \frac{r}{R} \right) e^{-i\omega_n t} \quad (17)$$

Where δz_n is the complex amplitude dynamical elongation at the center. For the fundamental mode $\lambda_0 = 2.405$.

During the vibration of this membrane, the frequency of oscillation f_0 can be described by a harmonic oscillator with a spring constant k and an effective mass m ;

$$f_0 = \frac{1}{2\pi} \sqrt{\frac{k}{m_{eff}}} \quad (18)$$

The spring constant can be obtained by second order differentiation of the total potential energy, with the elastic U_{el} and electrostatic contribution U_c and the effective mass can be obtained from the Kinetic energy U_{cin} expression

$$U_{cin} = \frac{1}{2} m_{eff} \delta z^2 \quad (19)$$

And also

$$U_{cin} = \frac{\rho}{2} \int_0^{2\pi} \int_0^R w(r)^2 r dr d\theta = 2\pi \frac{\rho}{2} \int_0^R \left(\delta z \cdot J_0 \left(2.405 \frac{r}{R} \right) \right)^2 r dr \quad (20)$$

$$U_{cin} = 0.136\pi\rho R^2 \delta z^2$$

It gives:

$$m_{eff} = 0.271\rho\pi R^2 \quad (21)$$

The spring constant is defined as $k = \partial^2(U_{el} + U_C)/\partial z^2$, if we take the equation 10 and 13;

$$U_{el} = \frac{1}{2} \cdot z^2 \cdot 2\pi \cdot T(z) + U_{init} \quad (22)$$

From this equation and equation 13, we will derive the spring constant as

$k = T_0 + \frac{12}{3} \frac{Et}{(1-\nu^2)R^2} \frac{z^2}{R^2} - \frac{1}{2} C'' V_g^2 = T_2$ with a renormalized tension T_2 , compare to T , which take into account the z dependence of T and the capacitive softening. We can write the resonant frequency of the fundamental mode as

$$f_0 = \frac{2.405}{2\pi R} \sqrt{\frac{T_2}{\rho}} \quad (23)$$

$$f_0 = \frac{1}{2\pi} \sqrt{\frac{2.405^2 \left(T_0 + \frac{12}{3} \frac{E}{(1-\nu^2)R^2} \frac{z^2}{R^2} \right)}{R^2 \rho} - \frac{\epsilon_0 V_g^2}{0,271 \times 3 \cdot d^3 \cdot \rho}} \quad (24)$$

If we integrate in this equation, the bending of the membrane, define in the equation 11, we obtain an expression as;

$$f_0 = \frac{1}{2\pi} \sqrt{2.405^4 \frac{Et^3}{12(1-\nu^2)R^4\rho} + 2.405^2 \frac{T_0}{R^2\rho} + 2.405^2 \frac{12}{3} \frac{Et}{(1-\nu^2)R^4\rho} \frac{z^2}{R^2} - 1.23 \frac{\epsilon_0 V_g^2}{d^3 \rho}} \quad (25)$$

And z is defined by the equation 14.

S4: Mechanical hardening and softening

The list of potential candidates related to a shift of a nanoresonator frequency are quite long; as a dopant absorption, an electrostatic force, a chemical potential variation, a chemical reaction, a photothermal effect, a joule heating, a slip of the MoS₂ at the clamped side, a defect diffusion, all nonlinear mechanical behaviors, an internal strain variation due to a crystal phase transition, a polarized piezoelectric effect. We investigate and explain our unique behaviors as the strong mode softening under the light of these different scenarios.

For our knowledge, in this list, only a few scenarios explain an in-plane strain shift; a phase transition, the piezoelectric effect and a dielectric polarization force induced by an in plane ununiformed polarization P or electric field¹⁶. But only the phase transition can be applied to our case and is strong enough to explain the 2.7 reduction in mechanical frequency.

Mass deposition:

Atomically thin mechanical resonators are well known to be mass sensitive but the MoS₂ is relatively heavy (160 Daltons per atomic mesh). The molecular absorption hardly explains our frequency reduction. It corresponds to the absorption and desorption of more or less 30-56 layers of water molecules, for example, on top of the MoS₂¹⁷. Consequently, the hysteretic

softening is related to the strain itself. Absorption-desorption is not excluded by a strong decrease of strain but considering that ions incorporation is usually hardening a material and is not reversible in a vacuum environment, it contradicts our observation.

In detail; We can consider the case of additional dopant absorption in or on the semiconductor. The sample is in high vacuum ($P \sim 1.10^{-5}$ mBar) but molecules like water or oxygen are still present in the cryostat and can affect the doping. We can put this scenario on one side if we consider the mechanical motion and reflection measurements. We consider a resonator of frequency $f = 1/2\pi \cdot (k/m)^{0.5}$, with m the effective mass of the resonator and k the spring constant. With mechanical motion detection, we are sensible to additional mass like within a chemical reaction or a layer deposition of absorbent. The dopant absorption, diffusion or desorption along the sample will modify f by δf and the additional mass will be $\delta m = 2m \cdot \delta f / f$ ¹⁸. If the frequency is reduced by 2 or 2.7 like in our mechanical memory measurements, it corresponds to an additional mass equivalent to 4-7 times the MoS₂ mass. It has been shown previously the possibility to fully recover a nanoresonators with layers of atoms¹⁷ but let consider this case. The mass of a mesh of MoS₂ $M_{\text{MoS}_2} = M_{\text{Mo}} + 2M_{\text{S}} = 160$ Daltons with $M_{\text{Mo}} = 96$ Daltons and $M_{\text{S}} = 32$ Daltons. The mass of a H₂O or O₂ molecules are 18 Daltons and 16 Daltons respectively. It means our frequency reduction corresponds to the absorption and desorption of more or less 30-56 molecules per mesh of MoS₂ and more than 30-56 layers of molecules on top of the MoS₂¹⁷. It is unlikely that this phenomenon is at the origin of our behaviors.

Capacitive softening

Mechanical hardening or softening are often observed in similar 2D devices or nanotube^{19,20} due to the sensitivity of these materials to external inputs. Indeed softening is related to the geometrical ratio between the membrane thickness t and the distance d to the gate electrode²¹, and is improve together with the electrostatic coupling, but a comparable strong softening was only observed in graphene resonators⁵ and attributed to a strong and attractive electrostatic force with a very close gate ($< 150\text{nm}$)²¹. Such a large reduction is expected when the capacitive force becomes comparable to the restoring force of the resonator. When the two forces are equal, the frequency drops to zero and the resonator collapses against the counter electrode. In our sample with large d , around 660nm, this capacitive softening is much less efficient. In fact, this mechanical hysteretic softening does not depend on the gate voltage, as shown in Figure 2c and at first glance is not related to capacitive softening.

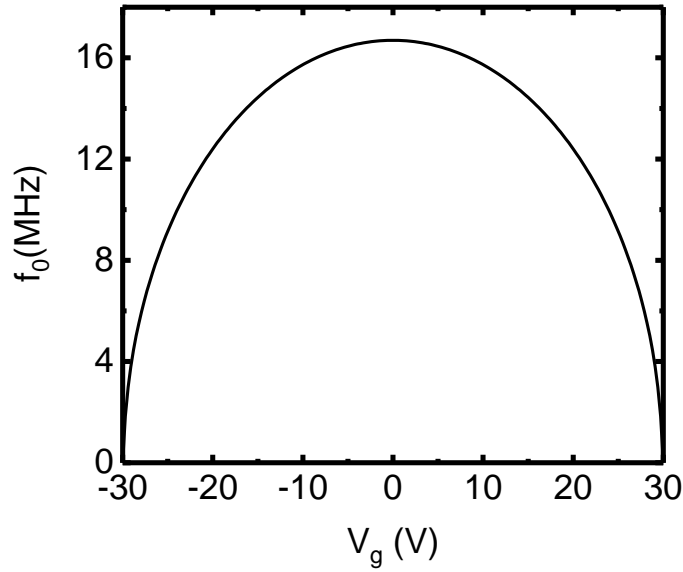


Figure S4a Capacitive softening simulation of the suspended MoS₂. We plot the capacitive softening term for the sample of Figure 2 in function of V_G (neglecting all others terms except the internal tension in equation 24). The memristive effect decrease the frequency at $V_H \sim 2.5V$ which is an order of magnitude more efficient than the capacitive term. Also the mechanical softening effect does not show any dependence in V_g but only in V_{ds} which is in contradiction with the capacitive softening term.

Heating:

Also, despite the threshold of the memristive effect appearing at the same power $P_H = I_H \cdot V_H$ independently from the photoconductivity (in Figure 2a and in SI), all the sample heating hypothesis can be easily ruled out. The photothermal effect induce by a laser of $10\mu W$ is negligible on our sample, as we have measure previously with Raman spectroscopy ¹, as well as the thermal dilatation. The Joule heating very small and heat the sample by few tens of degrees for an applied V_H and I_H , as shown in Figure 2b, and based on our COMSOL simulation (see SI). The temperature does not increase consequently, more than 177 K, if we remove the thermal coupling to SiO₂ pillars. However, since the temperature improve and higher V_{ds} polarization bring an out-of-equilibrium situation with hot electrons in the system, it certainly promotes the S_V diffusion or S_V clustering or a phase transition but the photocurrent and the mode softening are uncorrelated to any heating effect

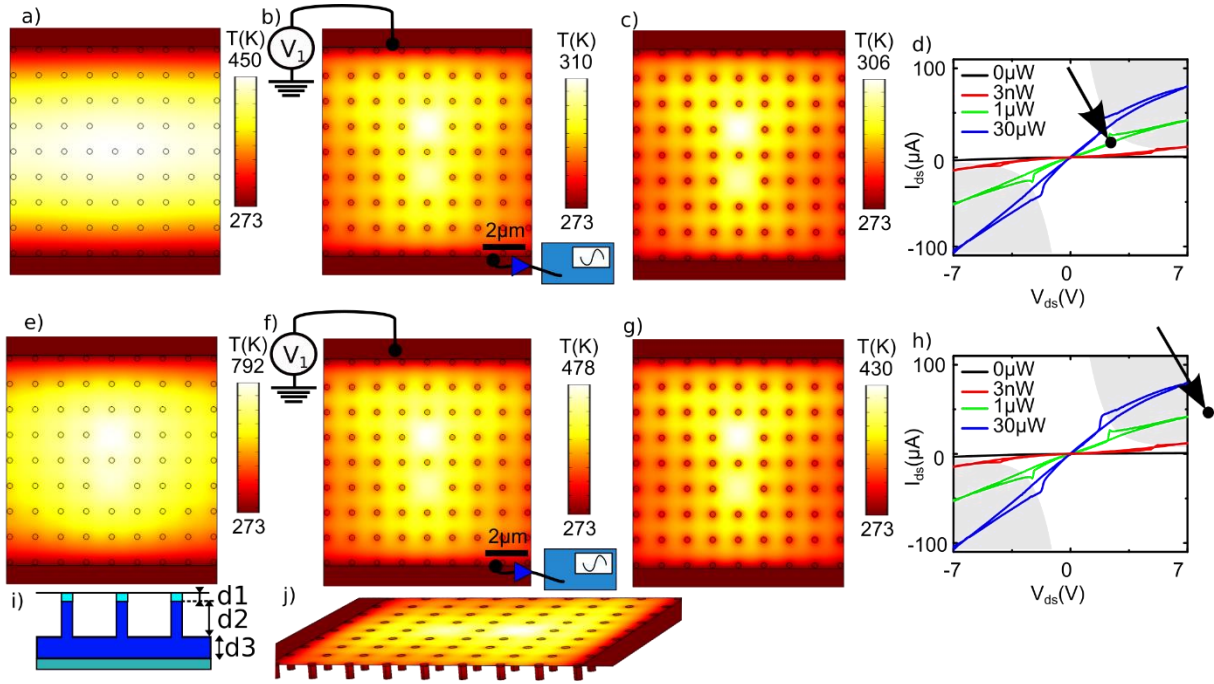


Figure S4b Joule heating in the suspended MoS₂. It is possible to heat the MoS₂ by Joule heating when a voltage is applied. a) b) and c) Joule heating, obtained with COMSOL simulation at $V_{ds}=2.4V$ and $I_{ds}=16\mu A$ as shown by the point in d) It corresponds to the jump in current in the memristive device. e) , f) and g) the Joule heating simulation at $V_{ds}=10V$ and $I_{ds}=42\mu A$. i) a schematic which shows the MoS₂ and the three different parts of SiO₂ with thickness $d_1=50nm$, $d_2=520$, $d_3=150nm$ and the Si substrate. j) the system under test with another point of view in order to see the pillars. We have changed the thermal coupling with the SiO₂ pillars by inserting a part d1 in the pillars structure with a reduced thermal conductivity k_{d1} . In a) it is $0W/m/K$, in b) and f) it is $k_{d1}=k_{SiO_2}/10$, in e) it is $k_{d1}=k_{SiO_2}/100$ and in c) and g) $k_{d1}=k_{SiO_2}$ with a perfect thermal coupling.

In the simulation, the MoS₂ is suspended with a thermal conductivity of $k_{MoS_2}=50W/m/K$, the SiO₂ pillars has a thermal conductivity of $k_{SiO_2}=1.4W/m/K$. It is possible to observe at the charge accumulation point that the power $P=I_{ds}\cdot V_{ds}$ only improve the temperature by few tens of degree. Even if the MoS₂ is completely decoupled from the pillars, the temperature only increase by 177 K which is not enough to explain a phase transition by Joule heating. We have also conducted some simulation with higher current and voltage and the temperature begin to rise if the decoupling to the SiO₂ pillars is quasi total. During the simulation the doping of the MoS₂ what convoluted with a Gaussian of $6\mu m$ of diameter in order to simulate the laser doping and placed at $x=0\mu m$ and $y=-1.26\mu m$, in the center of the larger membrane where the Joule effect is the strongest. The result is not strongly different than the case with a uniform doping. For the MoS₂ conductivity, only the voltage and the resulting current where fixed.

Sv diffusion along the membrane

In contrast, S_v centers were assumed to stress the material locally²², which is in contradiction with our observations. Additionally, our monocrystalline device exhibits this softening at the location of the laser excitation—far from the edges. If electromigration and Schottky barriers had a role to play in our samples, it would be conceptually different from ref²³, where ΔI_H decreased and the material degraded at the edges.

Membrane slipping

If we consider a membrane slipping on the anchoring, it can produce a mechanical relaxation of the build in strain but not a huge bipolar reversible effect. Our mechanical memristive behavior is not due to a slipping of the membrane

Piezoelectricity

Most of our device present some increase of frequency for high $|V_{ds}|$ and we assume it is a piezoelectric hardening of our suspended device. The in plane piezoelectric coefficient is $d_{11}=2.5-4$ pm/V and the out-of-plane ferroelectricity coefficient was recently measured to be $d_{33}=1.3$ pm/V (Two-dimensional materials with piezoelectric and ferroelectric functionalities) and at $V_{ds}=10V$ the additional strain is . If we consider this strain to be effective along the whole suspended MoS₂ and not only in our membrane under measurement, we will have to consider the stress applied on the membrane to be ?? which corresponds quite well to our data. Also, piezoelectricity presents a hysteresis in a strongly polarized material as a ferroelectric. 2H-MoS₂ is centrosymmetric and unfavorable to ferroelectricity and any intrinsic polarization. Even the 1T' phase, which presents a small out of plane polarization of $0.18\mu C/cm^2$ and a T_C at (ref Emergence of Ferroelectricity at a Metal-Semiconductor Transition in a 1T Monolayer of MoS₂ and <http://link.aps.org/supplemental/10.1103/PhysRevLett.112.157601>) does not explain this polarization. In a non-uniform distribution of charge as in a polarized dielectric material non uniformly doped by a laser, the associated current density corresponds to the movement of dipole moments density P as $J = \partial P / \partial t$. Since the dopants diffusion and current contribution is mostly associated to S_V vacancies and very long time scale in our sample, it is difficult to link any polarization to the relatively fast memristive behavior.

Dielectric force

Until now we have only consider electrostatic force to be capacitive coupling between two parallel plates with a uniform charge density. In reality, the semiconducting 2D material shows a high doping signature induced by the laser illumination and the charge density on the MoS₂ cannot be uniform anymore. It seems reasonable to approximate this density with a 2D Gaussian distribution. We consider a dielectric in a non-uniform electric field. The energy of an electrostatic system over a volume V is ²⁴

$$U_D = \frac{1}{2} \int_V \mathbf{D} \cdot \mathbf{E} dv = \frac{1}{2} \int_V \epsilon_0 \epsilon_R E^2 dv \quad (26)$$

It is possible to derive a Force F_D base on a dipole approximation. The force applied on a unique dipole with a small size compare to the rest of the system is;

$$F_{D1} = \mathbf{p} \cdot \nabla \mathbf{E} \quad (27)$$

A dielectric material can be approximate by multiple non interacting dipoles with a certain density and a corresponding macroscopic polarization density P . Then, if we consider a static electric field ($\nabla \times \mathbf{E} = 0$), the equation for a dielectric become

$$F_D = \mathbf{P} \cdot \nabla \mathbf{E} = \epsilon_0 \chi \mathbf{E} \cdot \nabla \mathbf{E} = \frac{1}{2} \epsilon_0 [(\epsilon_R - 1) \nabla \mathbf{E} \mathbf{E}] \quad (28)$$

$$F_D = \mathbf{P} \cdot \nabla \mathbf{E} = \epsilon_0 \chi \mathbf{E} \cdot \nabla \mathbf{E} = \frac{1}{2} \epsilon_0 [\nabla((\epsilon_R - 1) \mathbf{E} \mathbf{E}) - \mathbf{E} \cdot \nabla (\epsilon_R - 1)] \quad (29)$$

$\mathbf{E} \cdot \mathbf{E}$ is a tensor defined as

$$\mathbf{E}\mathbf{E} = \begin{pmatrix} E_x^2 & E_x E_y & E_x E_z \\ E_x E_y & E_y^2 & E_y E_z \\ E_x E_z & E_y E_z & E_z^2 \end{pmatrix} \quad (30)$$

$$\nabla = \begin{pmatrix} \partial/\partial x \\ \partial/\partial y \\ \partial/\partial z \end{pmatrix} \quad (31)$$

The term which is in plane can be consider as a pressure applied on a dielectric slab insert in the capacitor, of polarization density P, thickness t and width W. It represents for example some moving dopants along the MoS₂. The Force on the polarized plate, along x, would be

$$F \sim \frac{1}{2} \epsilon_0 (\epsilon_R - 1) \left(\frac{V}{d} \right)^2 W t \quad (32)$$

At the end, we have a strong analogy of this force with the capacitive force describe earlier. And the appearance of this force in the

S5: Relation between the reflectance and the cavity length.

In order to optimize the optical cavity length in between the MoS₂ and the substrate, we have defined the reflectance R on a laser at 633nm on the sample for both samples geometries. Sample A with d=520nm and d_{SiO₂}=150nm and sample B with d=440nm and d_{SiO₂}=220nm

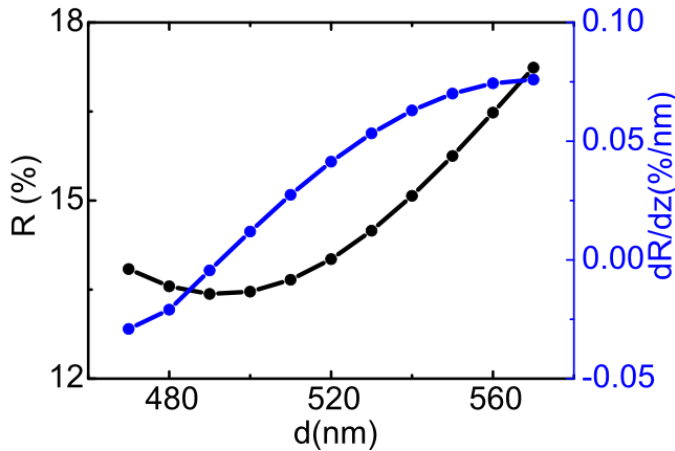


Figure S5 Relation between the reflectivity R and the cavity length d. We have plot the reflectance of the laser in function of the distance d between the MoS₂ and the SiO₂. In blue we have also plot the derivative dR/dz which is directly proportional to our mechanical signal amplitude. Here the SiO₂ thickness is 150nm and the MoS₂ is a monolayer flake. In this device, the SiO₂ thickness is 520nm with dR/dz at ~0.04%/nm.

S6: Memristor energy

The energy of a memristor during a step of current I_{ds} in the I_{ds}-V_{ds} curve is equivalent to a resistance energy with a times dependence of M(q(t)):

$$U_M = \frac{V_{ds}^2}{2} \int_{\Delta t}^0 \frac{1}{M(q(t))} dt = \frac{V_{ds}^2}{2} \int_{\Delta q}^0 \frac{1}{I_{ds} \cdot M(q)} dq = \frac{V_{ds}^2}{2} \frac{\Delta q}{V_{ds}} = \frac{1}{2} V_{ds} \Delta q \quad (33)$$

Since the energy does not depend on the deflection z and does not introduce a planar strain in the membrane, it will not directly intervene in the motion equation. But, for a fix V_g , and the gate charge equilibrium related to an external battery the capacitance energy will change by $U_C = 1/2 (q + \Delta q)^2 / C_g = 1/2 q^2 / C_g + q\Delta q / C_g$

In ref ²⁵, they consider the magnetic flux create by the moving dopant in the first memristor device ³. This magnetic flux is no null but 10^5 times lower than the magnetic flux created by the current charge. We will do the same in our system and neglect all magnetic force in our system, especially since the integration over a 2D space will gives lower values of the magnetic field.

S7: Persistent current measurements

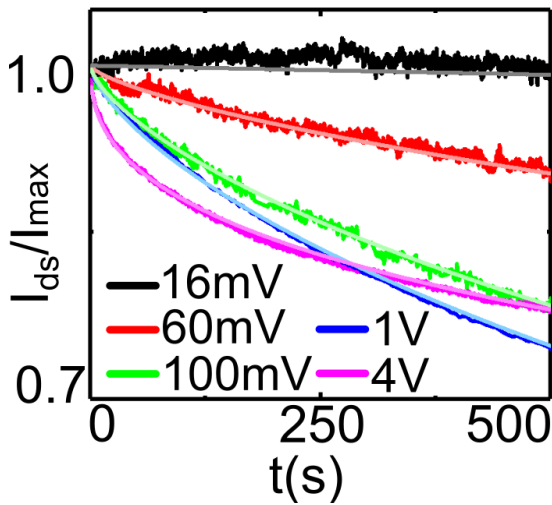


Figure S7 Time relaxation time of photocurrent at different V_{ds}

One can clearly notice that the relaxation time of the system strongly depends on the applied voltage. Thus, several regimes can be extracted: (i) at $V_{ds} = 16$ mV, the current was almost fixed at the same value when the excitation was OFF; (ii) around 60 mV, the long lasting relaxation time can be fitted by almost a single exponential function; (iii) between 100 mV and 1 V, the decay of the current can be fitted with good accuracy by means of a double exponential function, corresponding to a system with two types of traps or dynamics ($I(t) = I_1 e^{-t/\tau_1} + I_2 e^{-t/\tau_2}$)^{26,27}; (iv) beyond V_H (at $V_{ds} = 4$ V), we detect an additional contribution with a faster decay time $I(t) = I_1 e^{-t/\tau_1} + I_2 e^{-t/\tau_2} + \Delta I e^{-t/\tau_3}$, where τ_1 and τ_2 correspond to the long decay times in the order of 269 ± 48 s and 8815 ± 690 s, respectively, while τ_3 is relative to the fast decay time with a value around 20 s. Note that these PPC timescales were in accordance with previous studies^{27,28}. Furthermore, the contributions of ΔI , which is related to the memristive effect remained very low (4% of the total current) and difficult to analyze. To overcome this issue, we measured the I-V curve when the excitation was ON: we followed the dynamics of I_{ds} when the voltage was quickly swept from 0 V to a certain V_{ds} and then fixed at this value. After almost twelve seconds, the photocurrent generation I_{photo} dominate the measurements and is always positive for an extremely long time, independently from V_H . However, during the first ten seconds of the measurements, in Figure 4i, we observed again the appearance of a current assimilated to ΔI with the same dynamic and V_H dependence.

We have fit with exponential decay function with multiple decay time of the type $I(t) = I_1 e^{-t/\tau_1} + I_2 e^{-t/\tau_2} + I_3 e^{-t/\tau_3}$. Except the measurement at 16mV, most of the measurements where much longer than 500s and the fit for the long time scale (~ 8000 s) is quite accurate.

τ_1, τ_2, τ_3 are in seconds and the current is normalized at 1 for $t=0s$

At $V_{ds}=16mV$, $I(t) = 1e^{-t/60000}$.

At $V_{ds}=60mV$, $I(t)=0.04 e^{-t/287}+0.95 e^{-t/8300}$.

At $V_{ds}=100mV$, $I(t)=0.184e^{-t/272}+0.802e^{-t/8921}$.

At $V_{ds}=1V$, $I(t)=0.248e^{-t/328}+0.737e^{-t/8180}$.

At $V_{ds}=4V$, $I(t)=0.125e^{-t/191}+0.81e^{-t/9922}+0.04e^{-t/19}$.

At $V_{ds}=60mV$, the contribution of I_1 is only 4% of the total current and represents $18.6 \pm 5.3\%$ for higher V_{ds} . The contribution to the short time I_3 , at $V_{ds} = 4V$, is also very small at 4%.

S8: 1T' phase signature in our MoS₂ with Raman and photoemission spectroscopy

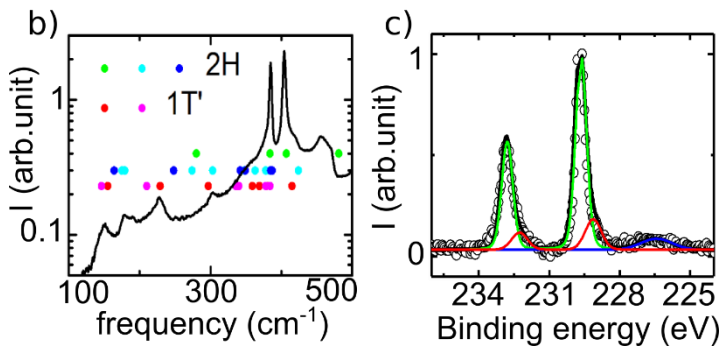


Figure S8 b) Raman spectroscopy of our MoS₂ at ambient conditions with the two main peaks of 2H-MoS₂ and small peak contributions from the 1T' phase. c) Photoemission signal of the MoS₂ with a main green peak contribution for the 2H phase and an additional red peak attributed to the 1T' phase. Both measurements indicated the presence of a few % of this phase in the material.

S9: Writing/ erasing processes and 1T' phase evidence in our MoS₂

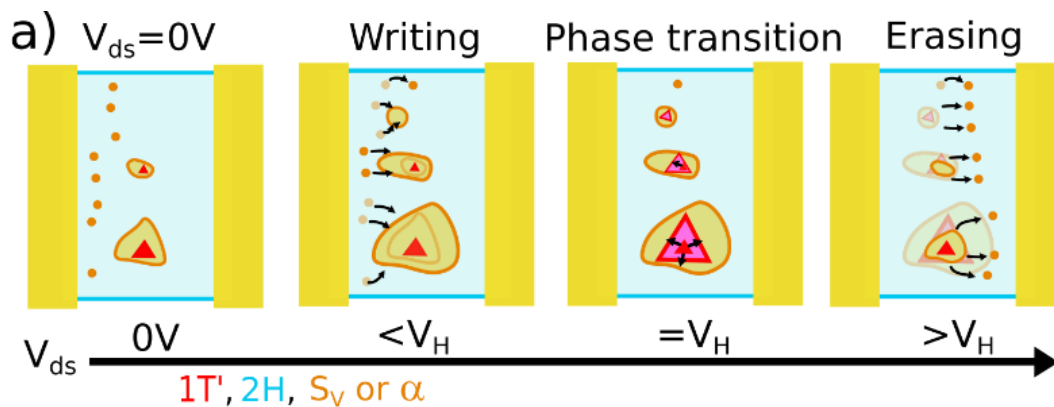


Figure S9 a) Schematic of the writing/erasing process for positive V_{ds} values. Below V_H , S_V centers migrated to the right and accumulated in or created α clusters. At V_H , the α phase promoted the nucleation of the phase 1T in the 2H phase. Beyond V_H , the field force exerted on S_V was strong enough to deplete clusters and decrease the presence of phase 1T which became unstable. The S_V were globally displaced to the left of the clusters and an opposite voltage, $-V_H$, was required to get them to migrate in the opposite direction, corresponding to a bipolarity of the memristive effect.

We demonstrate that S_V centers play a role in the slow dynamics of the memristive effect, to go further, we describe the interplay between S_V defects and phase transition which is measured mechanically. Similarly to other TMDs,²⁹ MoS₂ is a polymorph 2D material, presenting a memristive crystalline phase transition³⁰. The influence of some external parameters, such as doping, strain or electron injection, generate the nucleation of the metallic orthorhombic 1T phase of MoS₂ into the natural semiconducting 2H phase. This phase transition involves a sliding of S atoms in the unit cell. The new phase is unstable and can transit into different derivatives, like for instance to the disordered 1T' phase, due to charge density wave deformations. The formation energies are 0.84 eV for (2H→1T) and 0.55 eV for (2H→1T')³¹. However, to create a triangular island of 1T', this energy is insufficient: additional energy for 3 boundaries at the phase interface as well as the 3 corners is required. At the boundary between the two phases, in an S-poor MoS₂, there is a zig-zag chain or line of S vacancies³¹, also called the α phase. The total energy cost of the nucleation in a perfect 2H-MoS₂ is at less 6 eV³¹ which rarely occurs. However, a high density of defects, as S_V and a line of S_V , promotes the phase transition by strongly reducing this nucleation energy and weakening the Mo-S bonds, and by acting as electron donors which inject 0.04e in the nearby Mo atom²². Since the S vacancies were abundant in our MoS₂³² and since they participated in the 1T' nucleation process, we intuitively assigned a high concentration of sulfur vacancy to an energy formation reduction.

Figure S9 interprets the bipolarity of the memristive effect by arguing that the migration-drift of the S_V takes place in the preferential direction of the applied electric field, either in the writing phase, with the injection or the accumulation of the S_V centers in α phase, or in the erasing phase, with the S_V extraction of these clusters. Consequently, the S_V population on either side of the cluster is modulated with the polarization. The PPC is also in line with the slow drift of S_V centers acting as deep traps; their interaction with a depletion region as well as exciton dissociation and carrier collection, is favored if the S_V can move over a few μm , even if this movement is extremely slow³³, until it interacts with a metallic contact, for example, and is accelerated by an applied voltage.

References

- (1) Chaste, J.; Missaoui, A.; Huang, S.; Henck, H.; Ben Aziza, Z.; Ferlazzo, L.; Naylor, C.; Balan, A.; Johnson Jr, A. T. C.; Braive, R.; Ouerghi, A. Intrinsic Properties of Suspended MoS₂ on SiO₂/Si Pillar Arrays for Nanomechanics and Optics. *ACS Nano* **2018**, *12*, 3235–3242.
- (2) Kim, I. S.; Sangwan, V. K.; Jariwala, D.; Wood, J. D.; Park, S.; Chen, K.-S.; Shi, F.; Ruiz-Zepeda, F.; Ponce, A.; Jose-Yacaman, M.; Dravid, V. P.; Marks, T. J.; Hersam, M. C.; Lauhon, L. J. Influence of Stoichiometry on the Optical and Electrical Properties of Chemical Vapor Deposition Derived MoS₂. *ACS Nano* **2014**, *8*, 10551–10558.
- (3) Strukov, D. B.; Snider, G. S.; Stewart, D. R.; Williams, R. S. The Missing Memristor Found. *Nature* **2008**, *453*, 80–83.
- (4) Ge, R.; Wu, X.; Kim, M.; Shi, J.; Sonde, S.; Tao, L.; Zhang, Y.; Lee, J. C.; Akinwande, D. Atomristor: Nonvolatile Resistance Switching in Atomic Sheets of Transition Metal Dichalcogenides. *Nano Lett.* **2018**, *18*, 434–441.
- (5) Weber, P.; Güttinger, J.; Tsioutsios, I.; Chang, D. E.; Bachtold, A. Coupling Graphene Mechanical Resonators to Superconducting Microwave Cavities. *Nano Lett.* **2014**, *14*, 2854–2860.
- (6) Chen, C. Graphene NanoElectroMechanical Resonators and Oscillators, Columbia University, Columbia, **2013**.

- (7) Mei, T.; Lee, J.; Xu, Y.; Feng, P.; Mei, T.; Lee, J.; Xu, Y.; Feng, P. X.-L. Frequency Tuning of Graphene Nanoelectromechanical Resonators via Electrostatic Gating. *Micromachines* **2018**, *9*, 312.
- (8) Schomburg, W. K. *Introduction to Microsystem Design*, RWTH Edition Springer-Verlag: Berlin Heidelberg, Berlin, **2011**.
- (9) Weaver Jr., W.; Timoshenko, S. P.; Young, D. H. *Vibration Problems in Engineering*, John Wiley & Sons, New York, **1990**.
- (10) Storch, I. R. *Temperature-Dependent Mechanics in Suspended Graphene Systems*; Columbia university, Columbia, **2015**.
- (11) Fetter, A. L.; Walecka, J. D. *Theoretical Mechanics of Particles and Continua*; Dover Publications, Inc, New York, **2003**.
- (12) Schenck, D. R. Some Formation Problems for Linear Elastic Materials , Virginia Polytechnic Institute, Blacksburg, **2018**.
- (13) Chen, C.; Deshpande, V. V.; Koshino, M.; Lee, S.; Gondarenko, A.; MacDonald, A. H.; Kim, P.; Hone, J. Modulation of Mechanical Resonance by Chemical Potential Oscillation in Graphene. *Nat. Phys.* **2016**, *12*, 240–244.
- (14) Feynman R. P.; Leighton R. B.; Matthew S. The Feynman Lectures on Physics Vol. II Ch. 8: Electrostatic Energy, Addison-Wesley Publishing Company Inc., New york, **2017**.
- (15) Asmar, N. H. *Partial Differential Equations with Fourier Series and Boundary Value Problems: Third Edition*; Dover Publications Inc, New york, **2017**.
- (16) Unterreithmeier, Q. P.; Weig, E. M.; Kotthaus, J. P. Universal Transduction Scheme for Nanomechanical Systems Based on Dielectric Forces. *Nature* **2009**, *458*, 1001–1004.
- (17) Tavernarakis, A.; Chaste, J.; Eichler, A.; Ceballos, G.; Gordillo, M. C.; Boronat, J.; Bachtold, A. Atomic Monolayer Deposition on the Surface of Nanotube Mechanical Resonators. *Phys. Rev. Lett.* **2014**, *112*, 196103.
- (18) Chaste, J.; Eichler, A.; Moser, J.; Ceballos, G.; Rurali, R.; Bachtold, A. ANanomechanical Mass Sensor with Yoctogram Resolution. *Nat. Nanotechnol.* **2012**, *7*, 301–304.
- (19) Eichler, A.; Moser, J.; Chaste, J.; Zdrojek, M.; Wilson-Rae, I.; Bachtold, A. Nonlinear Damping in Mechanical Resonators Made from Carbon Nanotubes and Graphene. *Nat. Nanotechnol.* **2011**, *6*, 339–342.
- (20) Chen, C.; Rosenblatt, S.; Bolotin, K. I.; Kalb, W.; Kim, P.; Kymissis, I.; Stormer, H. L.; Heinz, T. F.; Hone, J. Performance of Monolayer Graphene Nanomechanical Resonators with Electrical Readout. *Nat. Nanotechnol.* **2009**, *4*, 861–867.
- (21) Sillanpää, M. A.; Khan, R.; Heikkilä, T. T.; Hakonen, P. J. Macroscopic Quantum Tunneling in Nanoelectromechanical Systems. *Phys. Rev. B* **2011**, *84*, 195433.
- (22) Gan, X.; Lee, L. Y. S.; Wong, K.; Lo, T. W.; Ho, K. H.; Lei, D. Y.; Zhao, H. 2H/1T Phase Transition of Multilayer MoS₂ by Electrochemical Incorporation of S Vacancies. *ACS Appl. Energy Mater.* **2018**, *1*, 4754–4765.
- (23) Sangwan, V. K.; Lee, H.-S.; Bergeron, H.; Balla, I.; Beck, M. E.; Chen, K.-S.; Hersam, M. C. Multi-Terminal Memtransistors from Polycrystalline Monolayer Molybdenum Disulfide. *Nature* **2018**, *554*, 500–504.
- (24) Fitzpatrick R. *Classical Electromagnetism*, University of Texas, Austin, **2018**.
- (25) Gale, E. The Missing Magnetic Flux in the HP Memristor Found. arxiv, **2011**, arXiv:1106.3170v1.
- (26) Amit, I.; Octon, T. J.; Townsend, N. J.; Reale, F.; Wright, C. D.; Mattevi, C.; Craciun, M. F.; Russo, S. Role of Charge Traps in the Performance of Atomically Thin Transistors. *Adv. Mater.* **2017**, *29*, 1605598.

- (27) Di Bartolomeo, A.; Genovese, L.; Foller, T.; Giubileo, F.; Luongo, G.; Croin, L.; Liang, S.-J.; Ang, L. K.; Schleberger, M. Electrical Transport and Persistent Photoconductivity in Monolayer MoS₂ Phototransistors. *Nanotechnology* **2017**, *28*, 214002.
- (28) Wu, Y.-C.; Liu, C.-H.; Chen, S.-Y.; Shih, F.-Y.; Ho, P.-H.; Chen, C.-W.; Liang, C.-T.; Wang, W.-H. Extrinsic Origin of Persistent Photoconductivity in Monolayer MoS₂ Field Effect Transistors. *Sci. Rep.* **2015**, *5*.
- (29) Yoshida, M.; Suzuki, R.; Zhang, Y.; Nakano, M.; Iwasa, Y. Memristive Phase Switching in Two-Dimensional 1T-TaS₂ Crystals. *Sci. Adv.* **2015**, *1*, e1500606.
- (30) Cheng, P.; Sun, K.; Hu, Y. H. Memristive Behavior and Ideal Memristor of 1T Phase MoS₂ Nanosheets. *Nano Lett.* **2016**, *16*, 572–576.
- (31) Zhao, W.; Ding, F. Energetics and Kinetics of Phase Transition between a 2H and a 1T MoS₂ Monolayer—A Theoretical Study. *Nanoscale* **2017**, *9*, 2301–2309.
- (32) Pierucci, D.; Henck, H.; Ben Aziza, Z.; Naylor, C. H.; Balan, A.; Rault, J. E.; Silly, M. G.; Dappe, Y. J.; Bertran, F.; Le Fèvre, P.; Sirotti, F.; Johnson, A. T. C.; Ouerghi,. Tunable Doping in Hydrogenated Single Layered Molybdenum Disulfide. *ACS Nano* **2017**, *11*, 1755–1761.
- (33) Sze, S. M.; Ng, K. K. *Physics of Semiconductor Devices*; John Wiley & Sons, Hoboken, **2006**.